Journal of Fluids and Structures 66 (2016) 293–314

Contents lists available at ScienceDirect

Journal of Fluids and Structures

journal homepage: www.elsevier.com/locate/jfs

On the near wake of a simplified heavy vehicle

Damien McArthur*, David Burton, Mark Thompson, John Sheridan

Department of Mechanical and Aerospace Engineering, Monash University, Clayton 3800, Australia

ARTICLE INFO

Article history:
Received 19 October 2015
Received in revised form
17 June 2016
Accepted 15 July 2016
Available online 18 August 2016

Keywords:
Bluff body
Wake
Heavy vehicle
Aerodynamics
PIV
Square back

ABSTRACT

Particle image velocimetry measurements of the near wake of a simplified generic truck geometry—the Ground Transportation System (GTS)—are presented. The mean flow field is characterised by a vertically asymmetric wake, with a large spanwise vortex in close proximity to the lower part of the base surface. Dominant non-dimensional frequencies of $St \approx 0.08$ and $St \approx 0.17$ are found, corresponding to a wake pumping mechanism and vortex shedding between the vertical edges of the base. Unsteadiness is largely confined to the top and side shear layers as well as the region downstream of the recirculating wake. In contrast, the lower region of the near wake is shown to remain almost quasi-steady, dominated by the persistent spanwise vortex that has a significant effect on the base pressure distribution. Ground proximity effects were assessed, showing that the wake topology is insensitive to increases in ground clearance, while a number of changes in flow regime were identified as ground clearance was reduced.

1. Introduction

Reducing heavy vehicle fuel consumption is an important challenge for both economic and environmental reasons. At a highway speed of 100 km/h aerodynamic drag comprises around 62% of the power required to propel a typical heavy truck (McCallen et al., 1999), with this proportion increasing with vehicle speed due to the quadratic relationship between drag and velocity. In fact, in the last few decades significant drag reductions have been achieved. A combination of better front-end aerodynamic design together with add-on devices have significantly reduced drag, especially that associated with the front of the vehicle (Burton et al., 2013; Leuschen et al., 2006). Reducing separation and improving the aerodynamic interaction between the cabin and trailer alone have been shown to result in large drag reductions (Martini et al., 2011). In addition, towards the rear of the vehicle side-skirts and wheel covers have been effective in maintaining attached flow and reducing stagnation on underbody components, as investigated by Ortega et al. (2008) and Landman et al. (2009).

With the advent and implementation of these technologies an increasing proportion of aerodynamic drag is now associated with the rear of the vehicle. Boat-tailing, i.e., extending the truck with angled surfaces, has been extensively investigated as a means of reducing wake drag (Burton et al., 2011; Kehs et al., 2013; Cooper, 2012), but has not been widely adopted for reasons of practicality. In order to continue to improve fuel consumption, new drag reduction strategies are required that will target this wake region.

Active flow control (AFC) shows promise as a means of base pressure recovery without the increased length or decreased cargo capacity required for boat-tails. One class of modern AFC methods aims to reduce the low pressure on the rear surface of the vehicle due to the proximity of wake vortices. Bruneau et al. (2010) used targeted blowing to move vortex cores away

* Corresponding author.
E-mail address: damien.j.mcarthur@gmail.com (D. McArthur).

http://dx.doi.org/10.1016/j.jfluidstructs.2016.07.011
0889-9746/

from the base of the vehicle, while Pastoor et al. (2008), Parkin et al. (2014), Parkin et al. (2015) and Phersson et al. (2014) used constant frequency suction and oscillatory blowing to force synchronous vortex shedding from both sides of a square-backed bluff body, causing large-scale vortices to form further downstream. While successful drag reduction has been achieved, particularly on two-dimensional bodies at low Reynolds numbers, it has yet to be shown that the same techniques are as useful for real heavy vehicles moving through a much more turbulent atmosphere at significantly higher Reynolds numbers.

The aspect ratio ($\mathcal{A}$ = length/width) of a separated wake is known to have a significant effect on bluff-body drag (Roshko, 1955). Bearman (1965) illuminated the importance of wake length as a parameter governing bluff body drag, finding an approximately linear correlation between base suction and the reciprocal of the vortex formation length. This showed that if the position where vortices begin to roll up is moved further downstream, their low pressure cores have less impact on the rear surface of the body. It has been shown that for bodies of revolution with a square back, a thicker separating boundary layer results in an increased base pressure, due to less momentum from the freestream flow being entrained into the wake, as described by Hoerner (1965) and more recently by Mariotti and Buresti (2013).

Another important component of the drag of three-dimensional bodies is induced drag (Hucho, 1998) associated with streamwise trailing vortices. For a lifting body, this component of the drag is proportional to the square of its lift. Han et al. (1992) found that this could be reduced by creating a balanced wake, hence minimising streamwise vortices.

To develop strategies to effectively modify heavy vehicle wakes and reduce their drag, it is necessary to improve our understanding of the typical flow structures present and their relationship to drag. Characterisation of the wake from both a mean and time-varying point-of-view may allow for a more targeted implementation of flow-control strategies. This knowledge can be gained most unambiguously through studying the wakes of simplified heavy vehicle geometries.

Significant research has been done on various square backed automotive geometries. Duell and George (1999) characterised the wake of an extruded rectangular square-backed body of unity aspect ratio with rounded leading edges in proximity to a moving ground plane. Two main unsteady motions were identified. The first was a quasi-periodic vortex emission from the wake at a non-dimensional frequency of $St = fW/U_\infty = 0.069$, with f being the dimensional frequency and U_∞ the free stream velocity. At this frequency the pressure peaks at the top and bottom of the base are almost 180° out of phase. Secondly they also found a higher frequency at $St = 1.157$ associated with shear-layer vortex shedding. Littlewood and Passmore (2010) performed PIV behind the Windsor model, describing the vortex-shedding process in the upper shear layer as a Markov Chain, suggesting that shedding may occur for a number of cycles, before being interrupted and remaining absent for a random period of time.

Another simplified automotive geometry that has received a large amount of attention recently is the square-backed *Ahmed* body. Grandemange et al. (2013b) was the first to find evidence of a lateral bistability in the wake at zero-degree yaw angle, with the flow switching seemingly randomly between two symmetrically opposite states on a time scale much longer than any observed vortex shedding period. While the time-averaged wake profile was found to be statistically symmetrical, the instantaneous flow fluctuated around one of the two asymmetric states. This behaviour was found to be dependent upon ground clearance (G), with bistable behaviour ceasing to occur below a critical height of $G/H = 0.1$. Away from the influence of a ground plane Grandemange et al. (2013a) found both vertical and horizontal bistabilities in the wakes of Ahmed bodies over a large range of aspect ratios, with the wake orientation generally switching between the two further apart edges of the geometry. Grandemange et al. (2014) also found that by placing a small vertical control cylinder in the symmetry plane of the wake approximately 0.7 H downstream of the base, the two bistable phases were no longer observed and the flow instead oscillated around a symmetrical topology. The result of suppressing this asymmetry was an increase in the mean recirculation length together with a drag reduction of 5.8%.

Volpe et al. (2014) found that over a range of yaw angles between $-1°$ and 1°, the probability distribution for the two wake states varied, while the structure of each state remained essentially the same. For yaw angles of magnitude >1° only one of the flow regimes was stable and the wake became permanently asymmetric. Also presented were conditionally averaged base-pressure contours and velocity fields for each state, as well as a spectral analysis of the wake dynamics for frequencies higher than that of the bistability switching mechanism. The dominant frequencies found were $St_H = 0.13$ and $St_H = 0.19$, were attributed to von Kármán shedding between the vertical and horizontal edges of the base, respectively. A low frequency peak was observed at $St_H \approx 0.07$–0.08, which was also found by Khalighi et al. (2001, 2012) and was likened to the low-frequency wake-pumping mechanism found by Duell and George (1999).

When compared to automotive vehicles, heavy vehicles have a larger height/width ratio as well as a significantly greater length. For these reasons simplified automotive models are not directly applicable to the study of heavy vehicle aerodynamics. To specifically develop drag reduction technologies for heavy vehicles a reference model is required that more accurately replicates these dimensions. The test geometry selected for this investigation is known as the *Ground Transportation System* (GTS). It features a smooth front end to minimise separation and an aspect ratio (height over width) of 1.39. The model has a total length of 7.65 W, the rearward 5.65 W of which is a constant section, finishing at a rectangular base with fixed separation lines (Croll et al., 1996). Storms et al. (2001) tested the original 1:8 scale model without wheels, finding laminar separation over the front edges at low Reynolds numbers, leading to a steep variation in drag coefficient below $Re_W = 1.0 \times 10^6$. Over the range of $3.5 \times 10^5 < Re_W < 2.0 \times 10^6$ the drag coefficient varied by 60% ($\Delta C_D = 0.31$), while the base pressure coefficient only changed by 2% ($\Delta C_{PBase} < 0.005$), suggesting that the Reynolds number sensitivity of the model is largely confined to the front of the vehicle. Base pressure measurements showed a low pressure over in the lower section of the base surface, extending in the spanwise direction to cover a region between $Y \pm 0.44$ W. Heineck and Walker

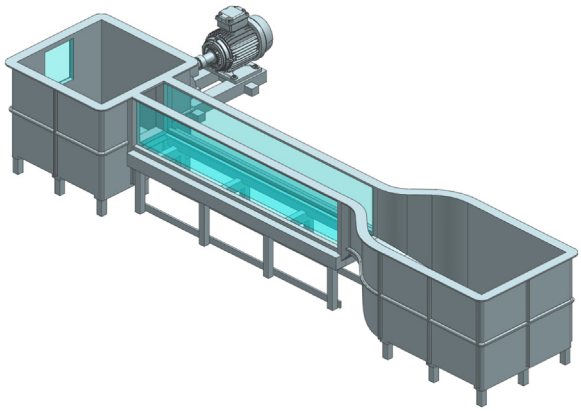

Fig. 1. The Monash University FLAIR recirculating water channel facility, showing the 4 m test section and 1D flow contraction. Laser sheets can be directed through the glass channel walls to facilitate PIV measurement in three sets of orthogonal planes.

(1999) performed 3D PIV on the model, but focussed on the measurement technology, rather than presenting detailed results and analysis of flow structures. Ortega et al. (2004) conducted Large Eddy Simulations over a truncated, rear section of the GTS with experimentally measured boundary layer profiles used as inlet conditions. Maddox et al. (2004), Unaune et al. (2005) and Roy et al. (2009) conducted Reynolds Averaged Navier Stokes (RANS) and Detached Eddy Simulations (DES) on the full GTS model, while Ghias et al. (2008) used an immersed boundary method with a realizable k–ϵ turbulence model. Of these computational approaches, the drag coefficients obtained from DES simulations more closely matched previous experimental results than those derived from calculations using RANS models; however, all computational methods have struggled to accurately capture the near-wake structures found experimentally. The simulations erroneously predicted that the mean near wake consisted of a ring vortex, with a plane of symmetry close to the half height of the model and a corresponding rear stagnation point at the centre of the base surface.

The current paper aims to document and elucidate both the steady state and transient near-wake structure of the GTS, and by doing so provide insight into possible alternate drag reduction strategies applicable to this class of flows as well as providing an extended dataset at achievable Reynolds numbers for future DES/LES-based computational studies.

2. Experimental setup

2.1. Test facility

The experiments detailed here were performed in the *Fluids Laboratory for Aerodynamic and Industrial Research* (FLAIR) water channel facility at Monash University (Fig. 1). The channel has a 4 m long test section with cross-section 0.6 m wide by 0.8 m high. The channel was filled to a depth of 0.78 m. Experiments were conducted at free-stream velocity of $U_0 = 0.42$ m/s, resulting in a Reynolds number of $Re_W = \rho U_0 W/\mu = 2.7 \times 10^4$ based on the width of the model. The channel has a free stream turbulence intensity (I_{uu}) of less than 1% and a velocity uniformity better than ±0.5%.

2.2. Experimental model

The model used for this investigation was a 1:40 scale GTS with length $L = 495$ mm, height $H = 90$ mm and width $W = 64$ mm (Fig. 2). The model was machined out of acetyl with the rearmost 25 mm of the model being made out of a clear

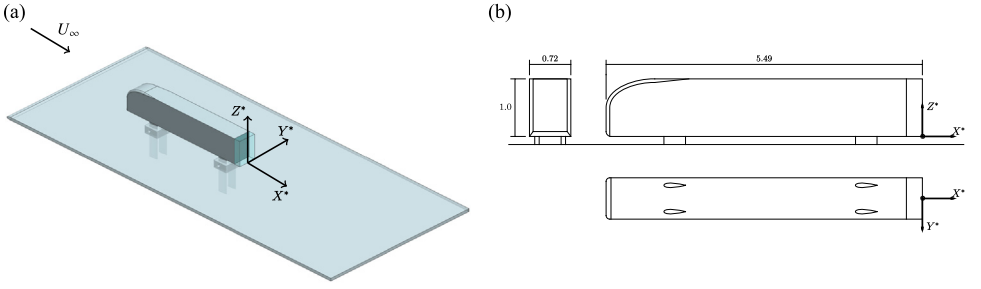

Fig. 2. 1:40 scale GTS model with ground plane and NACA0021 supports: (a) isometric view, (b) 3rd angle projection views, overall dimensions normalised by model height.

acrylic to allow transmission of the PIV laser. The model was placed upside down at a nominal ground clearance of $G^* = G/H = 0.14$ above a ground plane, which extended 2.5 H in front of the model and 7.5 H behind the model. The leading edge of the ground plane had an elliptical profile and the boundary layer thickness at the front of the model was measured at 0.09 H. Circular cylinders are often used as supports for simplified vehicle models, these are known to shed vortices and can introduce frequencies into the wake that are not characteristic of the base of the model. To alleviate this, the four model supports were replaced with NACA 0021 symmetrical airfoil profiles of thickness 0.079 H. While this simplification may not be geometrically representative of real world vehicles, it allowed for a clearer understanding of the idealised wake, as well as reducing flow unsteadiness beneath the vehicle, helping facilitate computational reproduction of this work. The supports protruded through the ground-plane and were secured on the other side to allow adjustment of the ground clearance between $G^* \approx 0.03$ and $G^* = 1.1$. The origin for the coordinate system used throughout this paper is located half way along the lower edge of the rearward face of the model as shown in Fig. 2. The X-axis points downstream, the Z-axis points vertically towards the top of the model and the Y-axis follows from a conventional orthogonal system. Unless otherwise noted, all dimensions are normalised by the model height H, such that $X^* = X/H$, $Y^* = Y/H$ and $Z^* = Z/H$. Exceptions to this are for the Reynolds and Strouhal numbers, which are normalised by model width following the convention of Storms et al. (2001).

2.3. Measurement techniques

Velocity fields in the *xz*, *xy* and *yz* planes of the wake of the model were obtained using particle image velocimetry (PIV). The flow was seeded with spherical glass particles with mean diameter 56 μm and density 1.016 g/cm^3 (Vestosint, Germany).

The flow was illuminated by a 532 nm, 5 W continuous laser (Changchun New Industries, China), which passed through a cylindrical glass lens to spread the beam into a planar sheet. It was imaged using a PCO.Dimax S CCD camera with resolution 2016 × 2016 12-bit pixels and maximum frame rate of 1000 frames per second. Image pairs were taken at a rate of 10 Hz, corresponding to a non-dimensional sampling frequency (Strouhal number) of $St = fW/U_0 = 1.5$. A 50 mm Nikon lens was used for imaging in the *xz* plane, while images in the *xy* and *yz* planes were captured through a 105 mm Nikon lens. For the *yz* planes the camera was mounted at the side of the tunnel and the image was reflected off a mirror placed 530 mm (5.9 H) behind the measurement plane at 45° to the flow direction. Velocity fields were taken in the plane $Y^* = 0$, with and without the presence of the mirror to confirm that it did not have a significant effect on the flow topology. With the mirror installed, the time-averaged wake closure point and upper vortex were displaced downstream by 0.01 H and 0.02 H respectively, while the location of the lower vortex remained unchanged. This minimal effect was deemed acceptable.

In addition to the high-speed imaging, PIV velocity fields shown in Figs. 5(b), 7 and 22–25 were obtained using two Nd:YAG 532 nm, 25 mJ Minilite II Continuum lasers from New Wave Research Inc., USA, and PIV frames were captured with a PCO.2000 CCD camera with 2048 × 2048 14-bit pixel resolution at a sampling rate of 0.5 Hz.

Velocity fields were obtained from image pairs using in-house cross-correlation-based software (Fouras et al., 2008). A final window size of 32 × 32 pixels, with a 75% overlap was used to compute velocity vectors. Magnification factors for the *xy*, *xz* and *yz* planes were typically 14.6, 13.1 and 12.4 px/mm, resulting in a vector spacing of 0.0068 H, 0.0061 H and 0.0071 H, respectively.

Convergence of the mean flow was assessed by monitoring the spatial mean of the Reynolds stress components in the $Y^* = 0$ and $X^* = 0.5$ planes, while temporally averaging over an increasing number of velocity fields (Fig. 3). All components of the spatially-averaged, time-averaged Reynolds shear stress converged to within $\Delta\overline{\langle u_x'^* u_y'^* \rangle} = 10^{-3}$ after 400 samples, as such a minimum of 500 instantaneous fields was considered sufficient to obtain mean velocity and Reynolds stress fields, although most data sets contain over 3200 instantaneous flowfields.

Convergence of the Proper Orthogonal Decomposition (POD) was also assessed. This was done by monitoring the kinetic

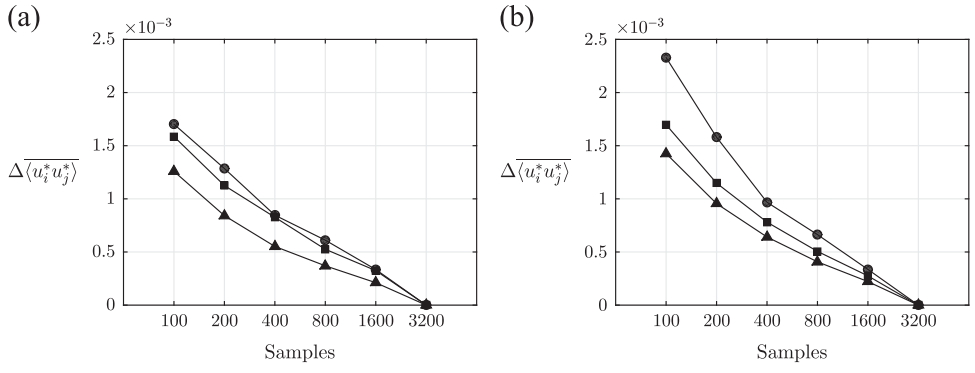

Fig. 3. Convergence of spatially averaged Reynolds stress magnitudes. (a) $Y^* = 0$ plane: • $\overline{\langle u_x'^{*2} \rangle}$, ■ $\overline{\langle u_z'^{*2} \rangle}$, ▲ $\overline{\langle u_x'^* u_z'^* \rangle}$, (b) $Z^* = 0.5$ plane: • $\overline{\langle u_x'^{*2} \rangle}$, ■ $\overline{\langle u_y'^{*2} \rangle}$, ▲ $\overline{\langle u_x'^* u_y'^* \rangle}$. Note $\langle \cdot \rangle$ denotes the time average and $\overline{\cdot}$ denotes the spatial average of the time averages.

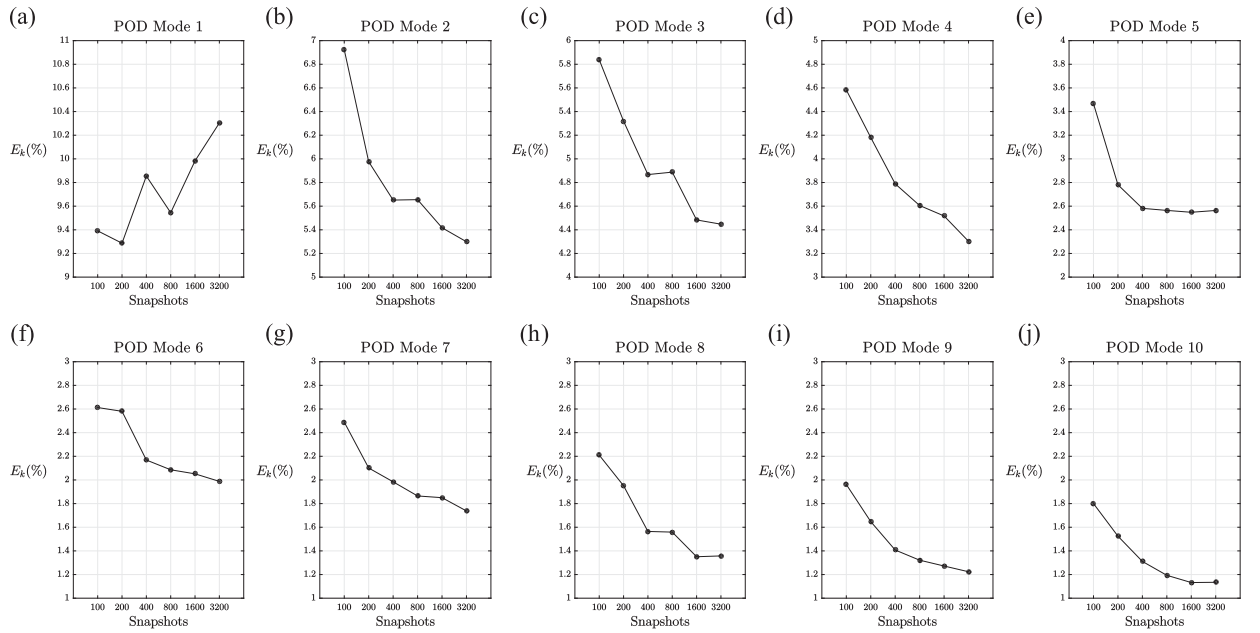

Fig. 4. Kinetic energy content of the first 10 unsteady POD modes: the points making up each curve correspond to using 100, 200, 400, 800, 1600 and 3200 snapshots for the decomposition.

energy distribution of the major contributing unsteady modes. Fig. 4 contains convergence plots for the fractions of total unsteady kinetic energy contained within each of the first 10 POD modes for sets of snapshots ranging from 100 to 3200. While this result does not show that the decomposition is fully converged, the trends indicate that accurate insights into the dominant flow structures can still be obtained. In addition, contour plots of the velocity magnitude for modes 1–5 for different numbers of snapshots are presented in the Appendix B. These show that even for a small number of snapshots, POD does a reasonable job of capturing the flow topology of the main modes. Frequency information was extracted from the fluctuating velocity field and the POD mode coefficients by calculating a power spectra. This was done on data sampled at 10 Hz using an FFT with a window size of 512 points and 75% overlap, zero padded to 1024 points. The resulting frequency precision was $\Delta St_w = 0.0015$.

To identify vortex structures the method of Graftieaux et al. (2001) is employed to calculate 2 variables Γ_1 and Γ_2 relating to the centre and bounds of a vortex respectively. The centre of a vortex can be found by calculating the local maximum of Γ_1, defined for any point P as:

$$\Gamma_1(P) = \frac{1}{N}\sum_S \frac{(PM \wedge (U_M))\cdot z}{\| PM \| \cdot \| U_M \|} = \frac{1}{N}\sum_S \sin(\theta_M)$$

where S is a rectangular region of interest surrounding P, containing N velocity vectors U_M, each located by the radius vector PM. While Γ_1 provides a convenient method for locating the centre of rotation of a vortex, it is not Galilean invariant, and as such is unsuitable for defining the bounds of a vortex core.

In order to overcome the problem of sensitivity to convection velocity, Γ_2 is introduced, which removes the local convection velocity $\tilde{U}_P = (1/N)\sum_S U dS$.

$$\Gamma_2(P) = \frac{1}{N}\sum_S \frac{(PM \wedge U_M - \tilde{U}_P)\cdot z}{\| PM \| \cdot \| U_M - \tilde{U}_P \|}$$

For values of $|\Gamma_2| > 2/\pi$ the flow is locally dominated by rotation and can be considered to be within a vortex core.

3. Results

3.1. Mean flowfield

The mean velocity field on the $Y^* = 0$ plane is presented in Fig. 5. The flowfield at the rear of the model consists of two main vortices, located at $(X^*, Z^*) = (0.21, 0.27)$ and $(0.60, 0.89)$, which rotate in opposite directions. The flow passing between the two main vortices stagnates on the base of the model at a height of $Z^* = 0.91$. This stagnation point is expected to correspond to the highest base pressure on the model, which agrees well with Croll et al. (1996), who measured the largest

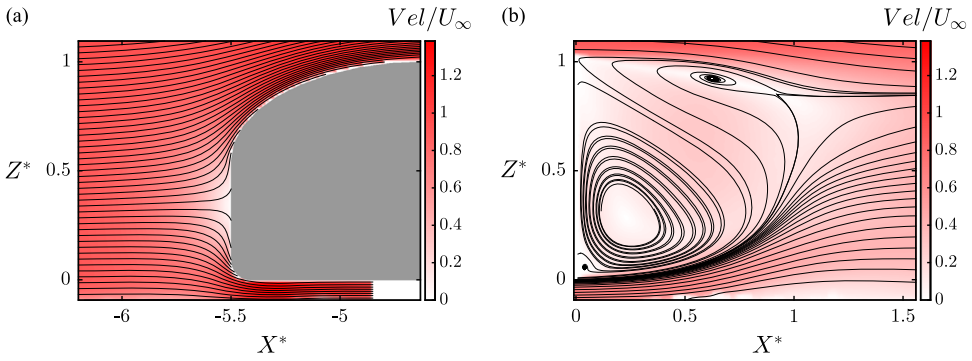

Fig. 5. Mean velocity overlaid with streamlines for the $Y^* = 0$ plane: (a) front of model, (b) rear of model.

base pressure in the vicinity of $Z^* = 0.9$. The lower pressure measured by Croll between $Z^* = 0.25$ and 0.5 can also be seen to be associated with the influence of the large lower vortex. The flow travelling downward along the base sees an adverse pressure gradient once it gets past the large vortex, and at $Z^* = 0.12$ the flow separates with a small vortex forming at $(X^*, Z^*) = (0.02, 0.05)$. The shear layer flow emanating from beneath the model exhibits a much greater streamline curvature than flow from above the model. Further downstream there is a saddle point at $(X^*, Z^*) = (0.88, 0.82)$ that divides the flow into 4 regions: flow passing between the two main vortices; the upper vortex; flow passing downstream above the upper vortex; and flow passing downstream from beneath the model. Another point of interest is the streamwise length of the recirculating wake (X_W) that we define as the distance from the base of the model to the furthest downstream point where the streamwise velocity component becomes zero. At the standard ground clearance this occurs at $X^* = 1.01$. Interestingly this is further downstream than the saddle point, consequently there is a region of flow near $(X^*, Z^*) = (0.96, 0.76)$, which emanates from beneath the model and becomes reversed without entering the time-averaged, recirculating wake. This flow topology shows remarkable similarity to the flow in the orthogonal *xy* plane of a square-back Ahmed body, when conditionally averaged over one of the two bistable states (Volpe et al., 2014). It should also be noted that the height-to-width aspect ratio of the square-back Ahmed body is approximately the reciprocal of the GTS ratio.

PIV data taken in planes parallel to the $Y^* = 0$ plane at a spacing of $H/30$ indicate that the main upper and lower vortices are persistent and clearly recognisable across 2/3 of the span of the vehicle. This is consistent with the base pressure measurements of Storms et al. (2001), who showed that the base pressure varied only minimally in the spanwise direction over 88% of the width.

Fig. 5(a) also shows mean velocity contours and overlaid streamlines in the symmetry plane at the nose of the model. As a result of the difference in shape between the large elliptical arc at the top of the model and the smaller radius at the bottom, the frontal stagnation point occurs lower than the centre of the model at a height of only $Z^* = 0.35$. It is apparent from this figure that the flow is fully attached over the top and bottom leading edges of the model, with a considerable speed-up present in the region between the lower leading edge and the ground plane.

The front-end velocity field in the plane $Z^* = 0.5$ on the other hand does show separation over the lateral leading-edge radius (Fig. 6a). This separation bubble extends approximately 0.5 H downstream and is consistent with the findings of Storms et al. (2001) for Reynolds numbers below $Re_w = 1.0 \times 10^6$.

At the rear of the body the flow in the $Z^* = 0.5$ plane is presented in Fig. 6(b). The wake region contains a symmetrical pair of vortices with cores located at $(X^*, Y^*) = (0.48, \pm 0.21)$. The separating streamlines from the lateral edges of the model bound the recirculating portion of the wake and join up at a saddle point at $(X^*, Y^*) = (0.895, 0)$.

Despite the reduced Reynolds number in the present study, the mean velocity fields including the time averaged critical

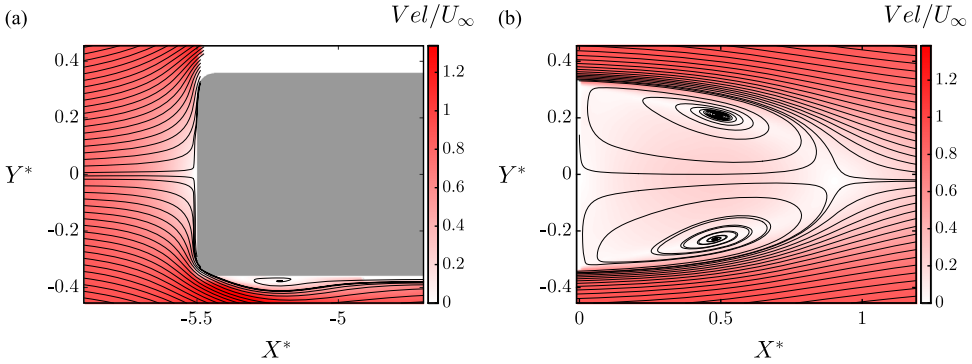

Fig. 6. Mean velocity overlaid with streamlines for the $Z^* = 0.5$ plane: (a) front of model, (b) rear of model.

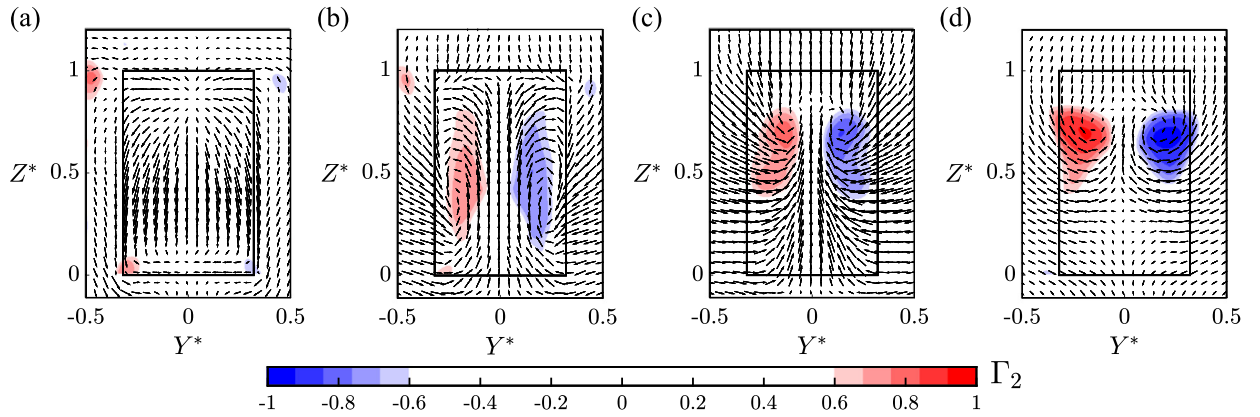

Fig. 7. Mean velocity vectors and Γ_2: (a) $X^* = 0.06$, (b) $X^* = 0.44$, (c) $X^* = 0.89$, (d) $X^* = 1.56$.

points in both Figs. 5(b) and 6(b) show strong agreement with the measurements at $Re_W = 2.0 \times 10^6$ by Storms et al. (2001), this comparison is presented in Appendix A. This finding is significant for numerical studies. While accurate simulations of the GTS at high Reynolds number are not feasible, the current dataset is within reach of well resolved Large Eddy Simulation such as Östh et al. (2014).

Fig. 7 contains mean velocity vectors and contours of Γ_2 in planes parallel to the base of the model at $X^* = 0.06$, 0.44, 0.89 and 1.56. Fig. 7(a) shows a stagnation point at approximately $(Y^*, Z^*) = (0, 0.9)$, as seen in Fig. 5(b). Further down the base, the flow has a significant negative vertical component in the region $0.2 \lesssim Z^* \lesssim 0.8$, consistent with the effects of the main lower vortex (Fig. 5b). The vertical component of velocity is largely independent of spanwise position in this region, providing further evidence that the effect of the main lower vortex is not confined to the centre of the wake. Towards the bottom of the base, flow is decelerated in accordance with the separation, and the secondary vortex region observed in the $Y^* = 0$ plane.

The plane at $X^* = 0.44$, cutting between the main upper and lower main vortices is shown in Fig. 5(b). Here the region behind the model contains a pair of elongated, counter-rotating vortices. The vortex pairs found in Figs. 5(b), 6(b) and 7(b) point to the time-averaged near wake consisting of a single large ring vortex, with its axis tilted at an angle to the freestream direction.

Fig. 7(c) and (d) shows a positive vertical velocity in the symmetry plane and the development of a pair of streamwise counter-rotating vortices, consistent with a body producing negative lift.

3.2. Vorticity

The out-of-plane vorticity components, $\omega_k = \frac{\partial u_j}{\partial i} - \frac{\partial u_i}{\partial j}$ are calculated by fitting a χ^2 polynomial to the velocity data to improve estimation of velocity gradients as described in Fouras and Soria (1998). Fig. 8 displays the time averaged, vorticity in the planes (a) $Y^* = 0$, (b) $Z^* = 0.5$, along with bounding streamlines and the time averaged main vortex locations. The upper and side vortex cores are located within the region of shear layer vorticity, while the main lower vortex is centred in a region of positive vorticity above the shear layer. A secondary region of negatively signed vorticity is generated on the base of the model in the $Y^* = 0$ plane by the flow induced by the main lower vortex. This flow separates at $Z^* = 0.12$ and the vorticity cross annihilates with positively signed vorticity in the lower shear layer.

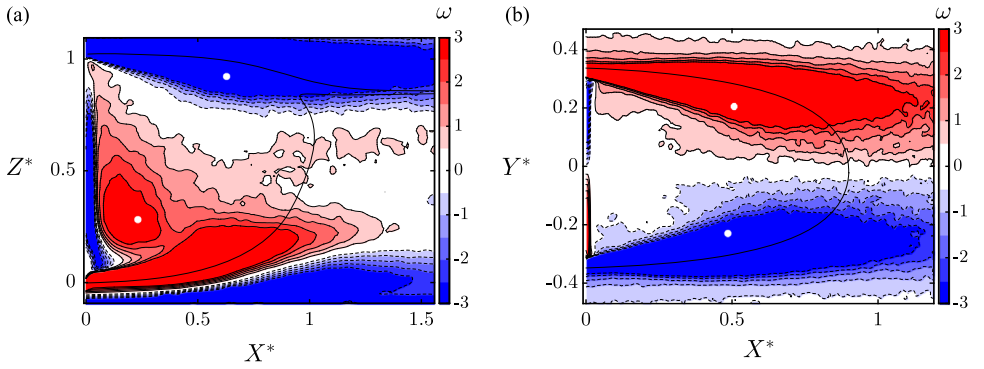

Fig. 8. Mean out-of-plane vorticity, overlaid with bounding streamlines. White circles denote the time averaged vortex locations. (a) $Y^* = 0$, (b) $Z^* = 0.5$. Colour axes have been truncated to show main lower vortex structure. (For interpretation of the references to colour in this figure caption, the reader is referred to the web version of this paper.)

It is important to point out that the levels in Fig. 8 were carefully selected to highlight the lower vortex structure and vorticity concentrations higher than those depicted do occur within the shear layers. While it may appear that the negative vorticity generated on the stationary ground plane is having an effect on the lower shear layer, the flow topology remains unchanged with increasing ground clearance as will be shown later in Fig. 22.

3.3. Reynolds stresses

The in-plane fluctuating Reynolds stress components for the flowfields at $Y^* = 0$ and $Z^* = 0.5$ are presented in Fig. 9. These are defined as the covariances of fluctuating velocity components, encompassing both large scale and random motions. The strongest component is the normal stress in the streamwise direction, with the largest values of $\langle u_x'^{*2} \rangle$ located along the upper (Fig. 9a) and side (Fig. 9b) shear layers. Fig. 9(c) shows a peak in the vertical fluctuations $\langle u_z'^{*2} \rangle$ occurring just downstream of the free saddle point, indicating that $\langle u_z'^{*2} \rangle$ results from an interaction between vorticity transported from the upper and lower shear layers. Similarly the peak in $\langle u_y'^{*2} \rangle$ is located downstream of the centre of the separated wake in Fig. 9(d), indicating that spanwise oscillations intensify beyond the time-averaged recirculating region. The regions of high Reynolds shear stresses, $\langle u_x'^* u_z'^* \rangle$ and $\langle u_x'^* u_y'^* \rangle$ (Fig. 9e and f), are collocated with the strongest intensities of $\langle u_x'^{*2} \rangle$. The sign of the shear stresses in these regions indicates that the main fluctuations are oriented at an angle inwards towards the centre of the wake, compared to the streamwise direction.

Three-dimensional representations of these fields were created by interpolating between parallel *xz* and *xy* planes. Fig. 10

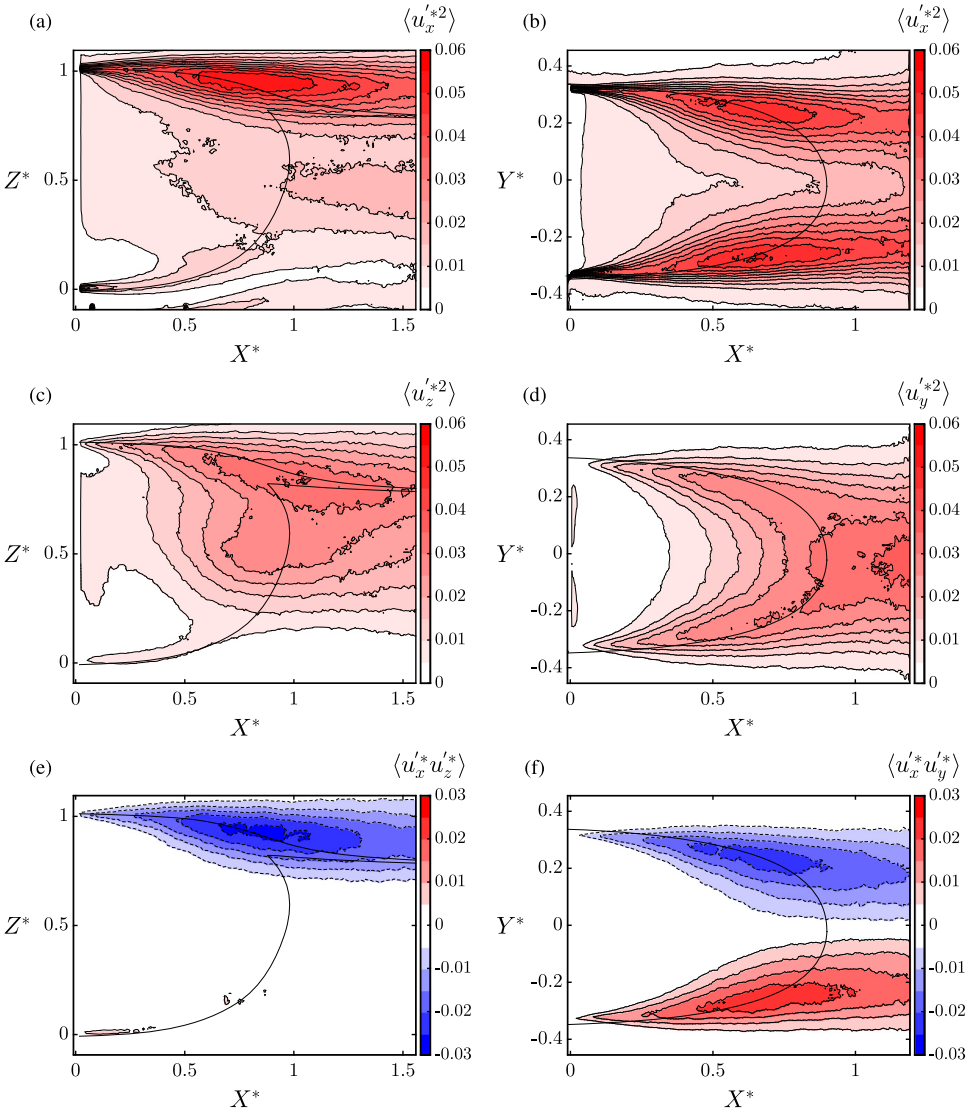

Fig. 9. Reynolds stress distributions overlaid with bounding streamlines. $Y^* = 0$ plane: (a) $\langle u_x'^{*2} \rangle$, (c) $\langle u_z'^{*2} \rangle$, (e) $\langle u_x'^* u_z'^* \rangle$. $Z^* = 0.5$ plane: (b) $\langle u_x'^{*2} \rangle$, (d) $\langle u_y'^{*2} \rangle$, (f) $\langle u_x'^* u_y'^* \rangle$.

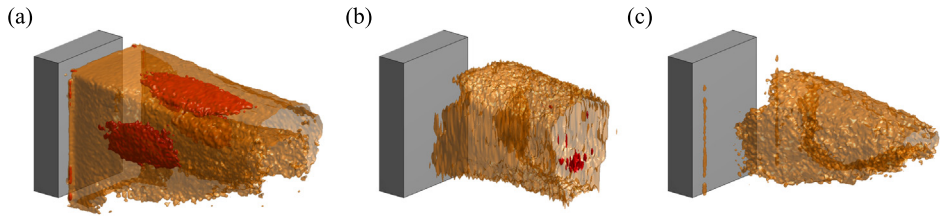

Fig. 10. Normal Reynolds stress distributions: (a) $\langle u_x'^{*2}\rangle$, (b) $\langle u_y'^{*2}\rangle$, (c) $\langle u_z'^{*2}\rangle$. Iso-surface levels: orange = 0.02, red = 0.04. (For interpretation of the references to colour in this figure caption, the reader is referred to the web version of this paper.)

contains the three normal Reynolds stresses, $\langle u_x'^{*2}\rangle$, $\langle u_y'^{*2}\rangle$ and $\langle u_z'^{*2}\rangle$. As seen before, $\langle u_x'^{*2}\rangle$ (Fig. 10a) is the strongest component, with peaks in the upper and side shear layers, $\langle u_x'^{*2}\rangle$ is reduced in the lower region of the side shear layers and is negligible in the flow emanating from beneath the model. Also worth noting is that the streamwise fluctuations are weaker downstream of the top corners of the model as compared to the upper shear layer at $y = 0$. The two remaining normal components $\langle u_y'^{*2}\rangle$ and $\langle u_z'^{*2}\rangle$ (Fig. 10b and c) are more strongly associated with the region in-between the free shear layers with $\langle u_z'^{*2}\rangle$ being stronger in the upper region of the wake. This suggests that the cross-stream normal Reynolds stresses, $\langle u_y'^{*2}\rangle$ and $\langle u_z'^{*2}\rangle$ occur largely as a result of interactions between opposing shear layers.

Two of the shear Reynolds stress components, $\langle u_x'^{*}u_y'^{*}\rangle$ and $\langle u_x'^{*}u_z'^{*}\rangle$, are presented in Fig. 11. The distributions of these are concentrated in the upper and side shear layers, as with $\langle u_x'^{*2}\rangle$, although at a smaller magnitude. The sign of $\langle u_x'^{*}u_y'^{*}\rangle$ is positive for $Y^* < 0$ and negative for $Y^* > 0$, indicating that positive streamwise fluctuations are correlated with an increase in lateral velocity inwards towards the centre of the wake. Similarly, $\langle u_z'^{*2}\rangle$ is negative throughout the upper shear layer, indicating that within the upper shear layer an increase in streamwise velocity is associated with a negative perturbation in the vertical flow.

3.4. Instantaneous flowfield

Velocity vectors of a typical instantaneous velocity field in the plane $Y^* = 0$ are overlaid on a contour plot of Γ_1 in Fig. 13 (a). The instantaneous field shows the main lower vortex in a similar location to the time-averaged field, while the upper shear layer is dominated by two discrete Kelvin–Helmholtz type vortices. The instantaneous wake at $Z^* = 0.5$ (Fig. 13b) shows considerable similarity with that of the upper part of the $Y^* = 0$ plane, with a number of identifiable small-scale vortices in each shear layer.

In order to track the distribution of these instantaneous vortices, the locations of the maximum and minimum values of Γ_1 were plotted over 3230 instantaneous PIV velocity fields (Fig. 12). This shows once again a strong similarity between the upper and side shear layers, with a distribution of shear layer vortices spreading downstream inside of the mean bounding streamlines. The position of the main lower vortex on the other hand is shown to be quite stable, spending the majority of the time close to its time-averaged position (Fig. 12a) .

It has been shown above that the lower shear layer has low levels of Reynolds stress and is not prone to the development of discrete vortices as found in the upper, and side shear layers. We propose that a cause of this is an inhibition of the Kelvin–Helmholtz instability, caused by a centrifugal acceleration of the flow towards the low pressure core of the main lower vortex.

Rayleigh (1917) showed that rotation acted to stabilise a fluid so long as the circulation of the fluid increased with radius, while linear stability analysis by Liou (1994) showed that for a curved free shear layer with radially increasing velocity, a reduction in radius of curvature leads to a reduction in the growth rate of both the Kelvin–Helmholtz and oblique instability modes.

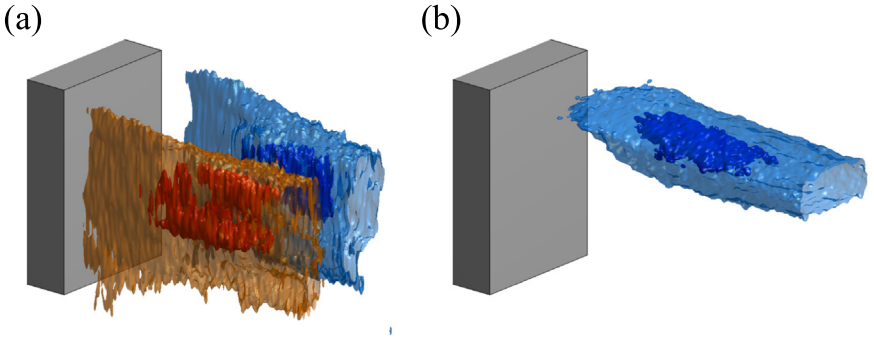

Fig. 11. Shear Reynolds stress distributions: (a) $\langle u_x'^{*}u_y'^{*}\rangle$, (b) $\langle u_x'^{*}u_z'^{*}\rangle$. Iso-surface levels: orange = 0.01, red = 0.02, light blue = -0.01, dark blue = -0.02. (For interpretation of the references to colour in this figure caption, the reader is referred to the web version of this paper.)

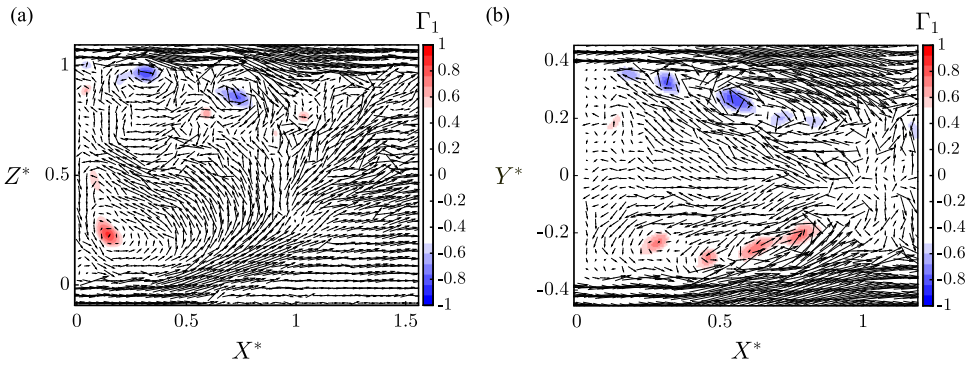

Fig. 12. Instantaneous velocity vectors and filled contours of Γ_1, (a) $Y^* = 0$, (b) $Z^* = 0.5$. Note that only every 25th vector is shown.

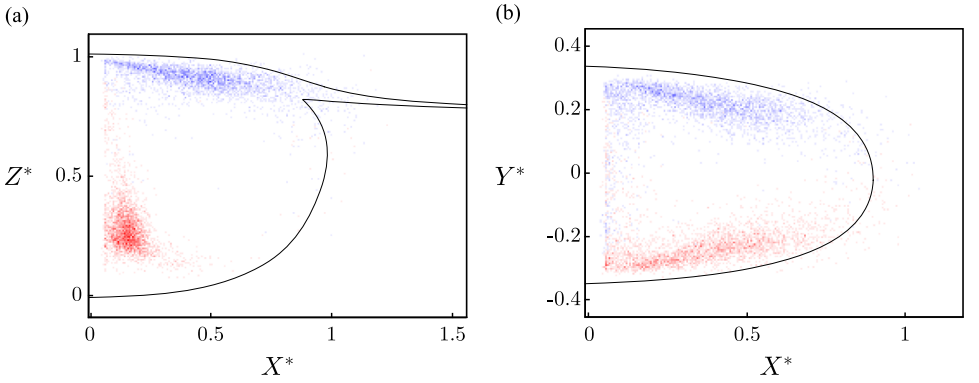

Fig. 13. Distribution of instantaneous Γ_1 maximum (red) and minimum (blue) location, overlaid with time-averaged bounding streamlines: (a) $Y^* = 0$, (b) $Z^* = 0.5$. (For interpretation of the references to colour in this figure caption, the reader is referred to the web version of this paper.)

While the local velocity profile in the lower shear layer does exhibit an inflection point, indicating that the Kelvin–Helmholtz instability will grow, the evidence above appears to suggest that the growth of this mode is hampered sufficiently that roll-up does not occur.

3.5. Frequency analysis

To assess the dominant dynamics of the wake structure, a discrete Fourier transform was constructed at each PIV point in the $Z^* = 0.5$ and $Y^* = 0$ planes using the FFT algorithm. Spatially averaged power spectra, normalised by the peak in-plane frequency are presented in Fig. 14. The $Z^* = 0.5$ plane (Fig. 14a) has a dominant peak at $St_w = 0.078$, with the streamwise component showing much greater intensity than the spanwise component. A secondary peak at $St_w = 0.17$ has comparable fluctuating energy in both directions. In the $Y^* = 0$ plane (Fig. 14b) a broader peak occurs around $St_w = 0.083$, although it is less dominant over the rest of the spectrum. These frequencies are comparable to those observed by Volpe et al. (2014), corresponding to the wake pumping mode (St_H=0.08) and vortex shedding between the two longer edges of the model (St_H=0.19).

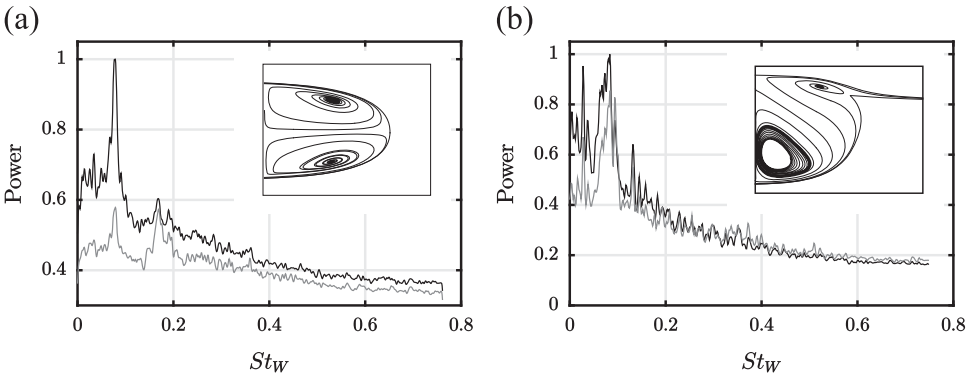

Fig. 14. Spatially averaged power spectra, (a) $Z^* = 0.5$, black = u', grey = v', (b) $Y^* = 0$, black = u', grey = w'. Power values normalised by local peak power.

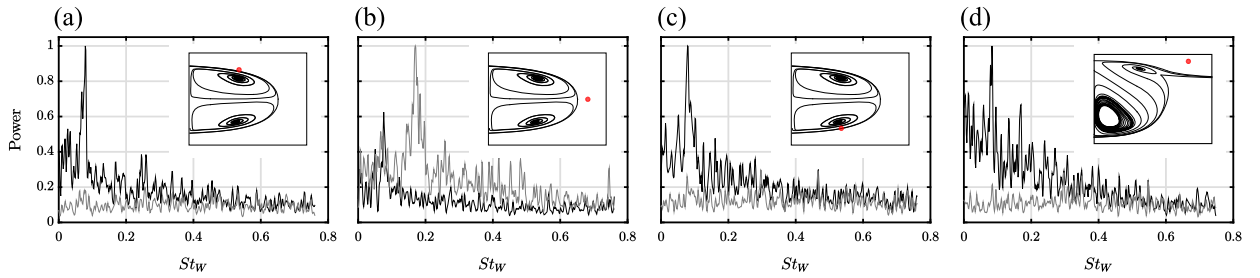

Fig. 15. Local power spectra, (a) $Z^* = 0.5$, $(X^*, Y^*) = (0.5, 0.3)$, (b) $(X^*, Y^*) = (1, 0)$, (c) $Z^* = 0.5$, $(X^*, Y^*) = (0.5, -0.3)$ black = u', grey = v', (d) $Y^* = 0$, $(X^*, Z^*) = (1.25, 1.0)$ black = u', grey = w'. Power values normalised by local peak power.

The sampling frequency of $St_w = 1.5$ is relatively low compared to some of the small-scale/high-frequency flow dynamics occurring in the wake of the GTS, particularly Kelvin Helmholtz-like vortex formation in the shear layers. To ensure the dominant frequencies identified was not the result of aliasing of fluctuations at higher than the Nyquist frequency, the plane at $Z^* = 0.5$ was repeated at a sampling rate of 100 Hz ($St_w = 15$). This produced the same dominant spectral peaks, confirming the validity of the results.

In an extensive study on the dominant frequencies around a 25° Ahmed body, Zhang et al. (2015) found that the frequency of certain wake motions was governed by vortices emitted from separation bubbles at the front of the model. This leads to changes in the wake periodicity when the frontal separation became suppressed at high Reynolds numbers. In the current work, frequency spectra were interrogated in the $Z^* = 0.5$ plane at the front and part way along the side of the model, confirming that the frontal separation region does not generate structures corresponding to either of the dominant wake frequencies identified above.

Power spectra at individual locations in Fig. 15 show that streamwise fluctuations around $St_w = 0.08$ dominate the sides of the wake (Fig. 15a and c) as well as downstream of the upper shear layer (Fig. 15d). While a peak in the spanwise velocity at $St_w = 0.17$ is located downstream of the centre of the wake at $Z^* = 0.5$ (Fig. 15b).

To better understand the motions associated with these dominant frequencies a technique introduced by Basley et al. (2011) was used whereby modal information can be extracted from PIV data by observing the spatial distribution of a particular frequency of interest. This was used to produce the power and phase angle distributions in the $Z^* = 0.5$ plane for $St_w = 0.078$ (Fig. 16) and $St_w = 0.17$ (Fig. 17) as well as in the $Y^* = 0$ plane for $St_w = 0.083$ (Fig. 18). The phase angle ϕ is

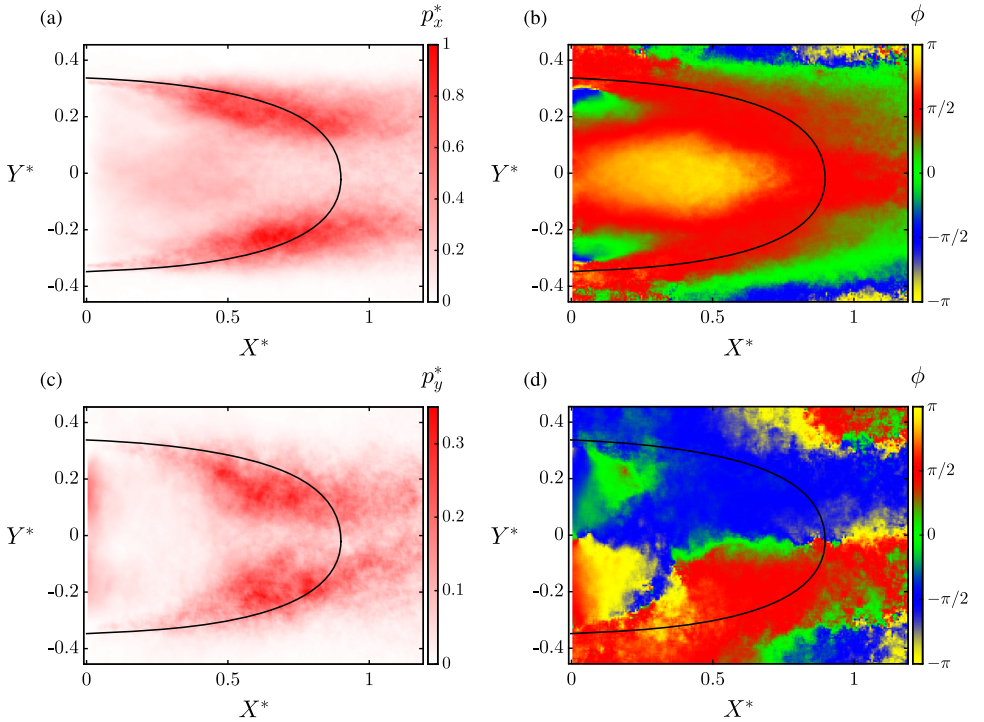

Fig. 16. Spatial distributions of mode at St_w=0.078 in plane $Z^* = 0.5$ overlaid with time averaged separating streamlines: (a) u' power, (b) u' phase, (c) v' power, (d) v' phase.

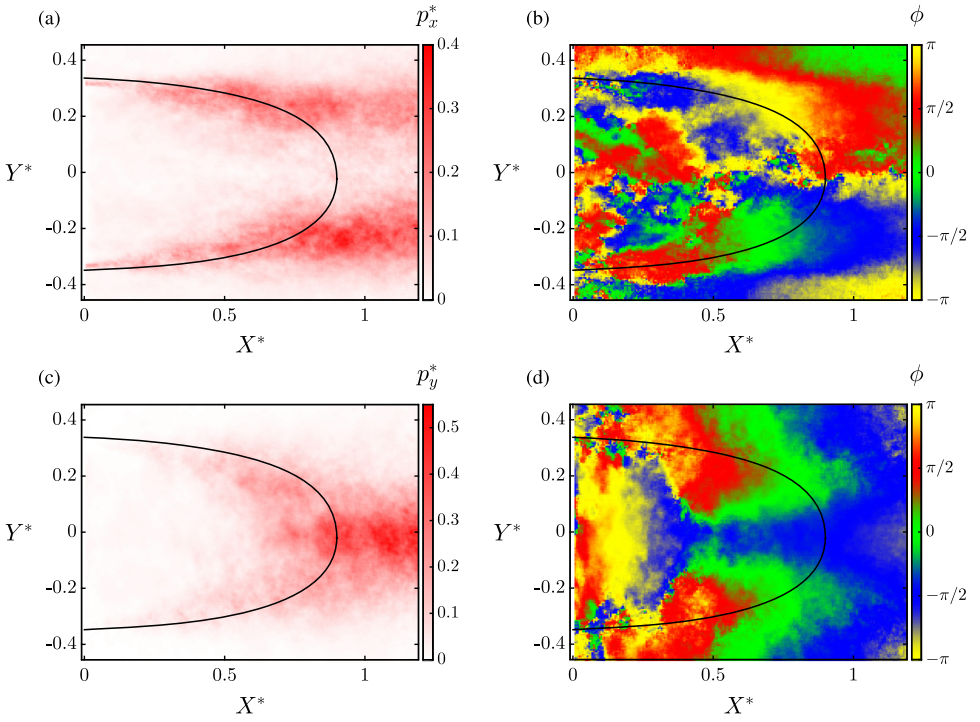

Fig. 17. Spatial distributions of mode at St_w=0.17 in plane Z^* = 0.5 overlaid with time averaged separating streamlines: (a) u' power, (b) u' phase, (c) v' power, (d) v' phase.

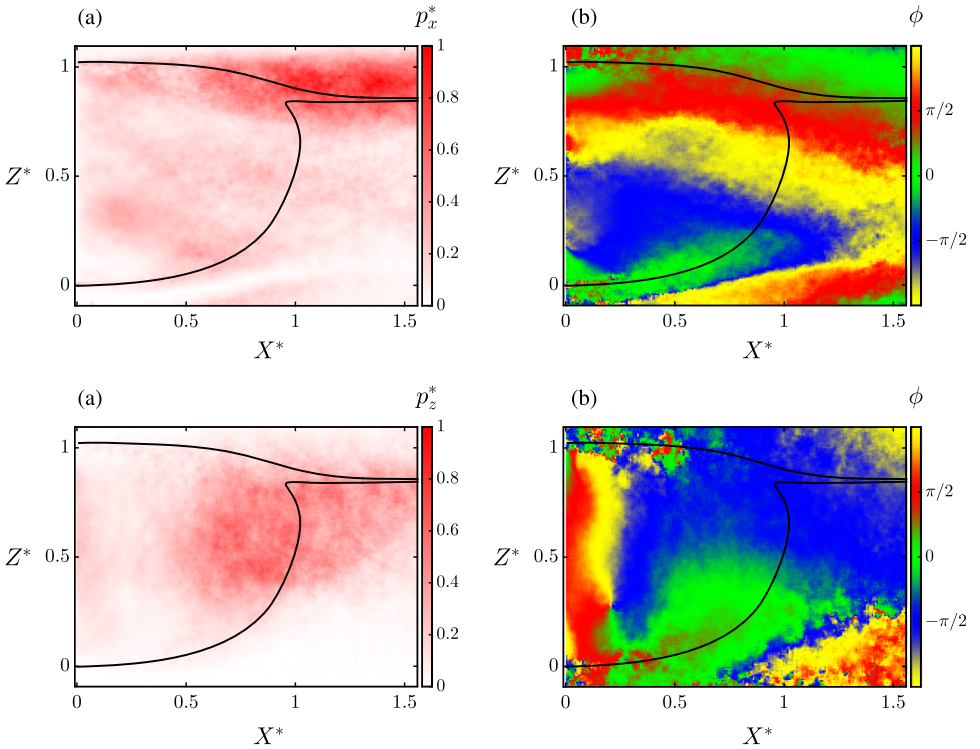

Fig. 18. Spatial distributions of mode at St_w=0.083 in plane Y^* = 0 overlaid with time averaged separating streamlines: (a) u' power, (b) u' phase, (c) w' power, (d) w' phase. (For interpretation of the references to colour in this figure caption, the reader is referred to the web version of this paper.)

plotted over a range from $[-\pi, \pi]$ with a circular colourmap comprising of 4 colours: red, yellow, blue and green, each separated by $\frac{\pi}{2}$.

The power distribution of both the u'(Fig. 16a) and v'(Fig. 16c) fluctuations in the $Z^* = 0.5$ plane at $St_w = 0.078$ is concentrated in the two side shear layers, in much the same region as the peaks of $\langle u_x'^{*2} \rangle$ and $\langle u_x'^* u_y'^* \rangle$. (Fig. 9b and f). The phase plots show that the streamwise fluctuations in both shear layers are in phase (Fig. 16b). The spanwise velocity in the shear layer for $Y^* < 0$ is also in phase with the bulk streamwise fluctuations, while for $Y^* > 0$ the spanwise velocity is 180° out of phase.

When the main streamwise fluctuations are at a maximum ($\phi \approx \pi/2$), the increase in streamwise and inwards velocity, corresponds to an increase in bounding streamline curvature and a contraction of the wake, with the wake closure point and main vortices appearing further upstream. By 180° later, the negative perturbation in the streamwise velocity corresponds to an expansion of the wake, with the main critical points being translated downstream. This motion, along with the particularly large regions of near constant phase, is consistent with a fluctuation in the bulk pressure within the wake and agrees both in frequency and structure with the wake pumping mechanism observed by Duell and George (1999) and Volpe et al. (2014).

The location of the streamwise fluctuations at $St_w = 0.17$ (Fig. 17a) is similar to those at $St_w = 0.078$, while the v component is strongest downstream of the centre of the wake and has a very similar distribution to $\langle u_y'^{*2} \rangle$ (Fig. 9d). Streamwise fluctuations on opposing sides of the wake are ≈180° out of phase (Fig. 17b) while spanwise fluctuations on opposing sides of $Y^* = 0$ are in phase. This is consistent with out of phase vortex shedding from opposing sides of the wake, as in the process of von Kármán shedding.

The $St_w = 0.083$ mode in the $Y^* = 0$ plane once again corresponds to the wake pumping mechanism. It has the strongest streamwise fluctuations in the upper shear layer and vertical fluctuations around the wake closure region as seen in Fig. 18. These, once again show similarity to the distributions of $\langle u_x'^{*2} \rangle$ and $\langle u_z'^{*2} \rangle$ respectively (Fig. 9a and c). The phase distributions in Fig. 18(b) and (d) illustrate that the u' fluctuations are in phase in the streamwise direction over the length of the wake, indicating that this frequency corresponds to a bulk change in the wake rather than a structure growing and convecting downstream.

3.6. Proper orthogonal decomposition

The main unsteady fluctuations in the flow were further characterised by the construction of a Proper Orthogonal Decomposition (POD) of the instantaneous time-resolved sequential velocity fields. POD involves breaking the flow-field up into a number of optimal, orthogonal spatial modes, based on their kinetic energy content. This method elucidates the more energetic flow structures and can be used as a filter to remove small-scale random turbulence and PIV uncertainties/errors. A review of the derivation and implementation of POD for turbulent flows can be found in Berkooz et al. (1993).

The POD was constructed on entire velocity fields, without subtracting the mean velocity. For both planes, a mode structurally equivalent to the mean flow was returned, which has been denoted here as Mode 0. In each case the power spectrum of Mode 0 contained a peak at the same frequency as Mode 1, as such neither the mode shapes nor power spectra have been presented.

The fraction of unsteady kinetic energy in each POD mode is equal to the eigenvalue of that mode. The relative strength of these modes is displayed as a percentage of the sum of the eigenvalues (excluding mode 0). The kinetic energy content modes 1–10 for both the $Y^* = 0$ and $Z^* = 0.5$ planes are presented in Fig. 19.

Both planes show similar distributions of energy through the dominant modes, with the $Y^* = 0$ and $Z^* = 0.5$ planes having respectively 23.3% and 21.9% of the unsteady kinetic energy within the first 4 modes. These levels are quite low compared with typical values reported for bodies whose aerodynamic loading is dominated by a single coherent large-scale motion. Van Oudheusden et al. (2005), for example, presented flow around a 2D square cylinder in which 75% of the unsteady energy was concentrated in only the first two modes.

The relatively low energy concentration within the first modes may be a consequence of the nonlinear interaction between the dominant modes in the wake. Interactions between two dominant modes, i.e., the wake pumping and vortex

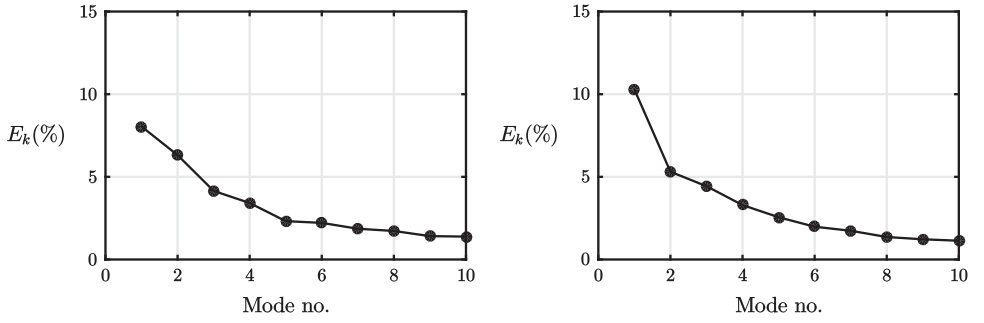

Fig. 19. Kinetic energy of the first 10 POD modes: (a) $Z^* = 0.5$, (b) $Y^* = 0$.

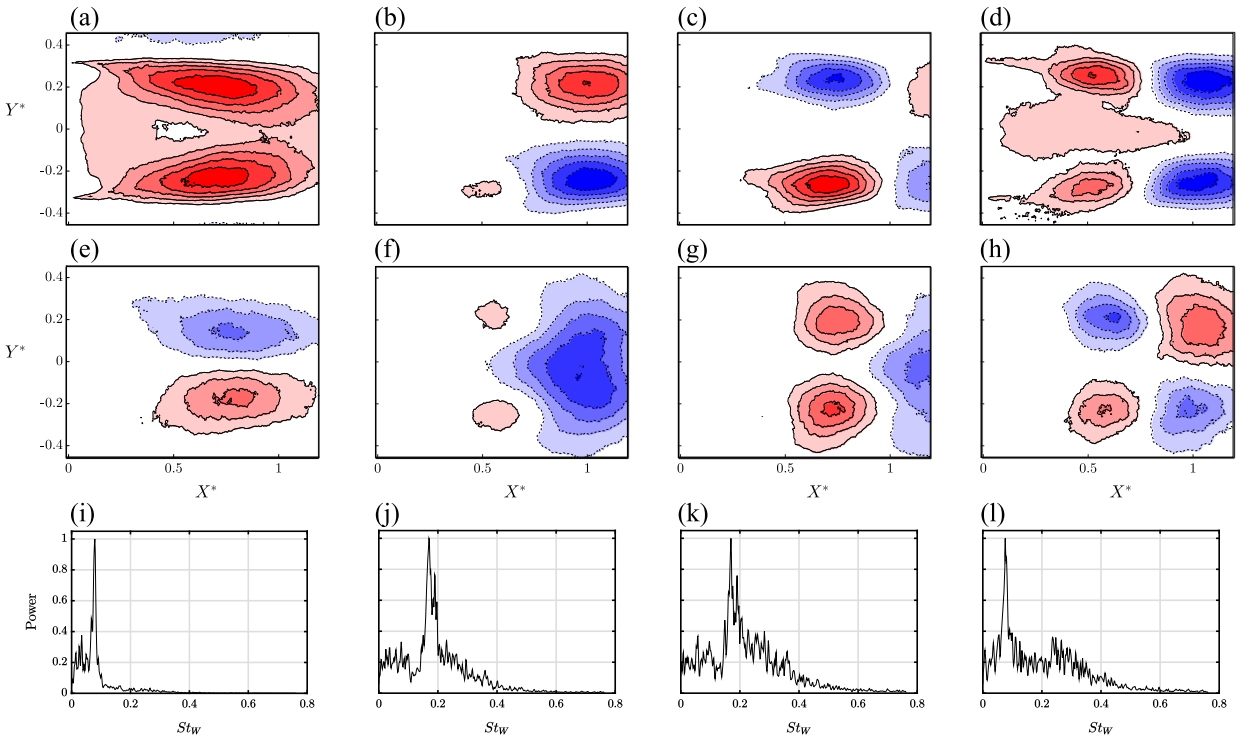

Fig. 20. Proper Orthogonal Decomposition of the $Z^* = 0.5$ plane. *U* velocity modes 1:4 (a–d), *V* velocity modes 1:4 (e–h), normalised power spectra of the mode coefficient, modes 1:4 (i–l). Contours normalised by peak mode component.

shedding modes, mean that the location and structure of fluctuations may not be consistent from cycle to cycle. This could mean the wake is less well described by just a few modes, with higher-order corrections necessary to represent any instantaneous wake state.

The first 4 POD modes in the $Z^* = 0.5$ plane are presented in Fig. 20. The first unsteady mode is symmetrical about the centre plane of the model and shows large-scale motions in the shear layers, dominated by the *U* velocity component. The power spectra of the time series of each mode's energy coefficient is displayed at the bottom of each column of subfigures. The Mode 1 spectrum shows a peak at a reduced frequency of $St = 0.078$, this corresponds once again to the wake pumping, shown from the Fourier spectrum (Fig. 16). Coupled with the mean mode (not shown) this is indicative of a periodic lengthening and shortening of the mean recirculation bubble. For the second mode, the *U* velocity component is anti-symmetric about $Y^* = 0$, while the *V* component is symmetric. This mode's spectrum shows a broad peak at $St = 0.17$, which is within the range of Strouhal numbers typically associated with the von Kármán instability. Mode 3 takes a similar form to Mode 2, with the main *U* component structures occurring further upstream and the sign of the *V* component being reversed with respect to the *U* structures. The coefficient spectrum for Mode 3 also shows the same peak, indicating a coupling between the two antisymmetric modes. While the lateral oscillations share some features with von Kármán vortex shedding, due to the highly complex and three-dimensional nature of the flow, the physical mechanism behind the fluctuations appears more complex than the 2D process described in Gerrard (1966). The fourth mode is once again symmetric about $Y^* = 0$, and contains structures similar to Mode 1 on a smaller spatial scale. The peak frequency for this mode appears the same as that of the wake pumping mode, thus it provides a correction mode 1 to account for variations seen between cycles.

Within the remaining POD modes there exist a number of symmetric and anti-symmetric modes with power spectra peaks around $St_w = 0.08$ and $St_w = 0.17$. As with mode 4, these presumably amount to modifications to the wake pumping and horizontal shedding modes necessary to reconstruct any instantaneous wake state. Higher-order modes with different mode coefficient frequency content probably account for less coherent/regular smaller scale structures and out-of-plane motions. However, because modes beyond mode 4 contain the majority of the unsteady kinetic energy content, this indicates that using only those first four modes will not provide the accurate reconstruction of any instantaneous wake state, even though it may provide a reasonable picture of the dominant physics.

Fig. 21 contains the unsteady modes in the $Y^* = 0$ plane. The first thing of note is that the velocity fluctuations in the higher power modes are largely confined to the upper shear layer, with flow in the lower portion of the wake exhibiting negligible levels of large-scale fluctuation. Mode 1 once again shows evidence of the bulk wake pumping, occurring at a frequency of $St = 0.083$, as does Mode 3. Modes 2 and 4 suggest smaller structures in the same region, with mode 2 displaying a frequency peak at $St = 0.13$. This pairing may relate to the shedding measured by Volpe et al. (2014) between the vertical edges of the square back Ahmed body.

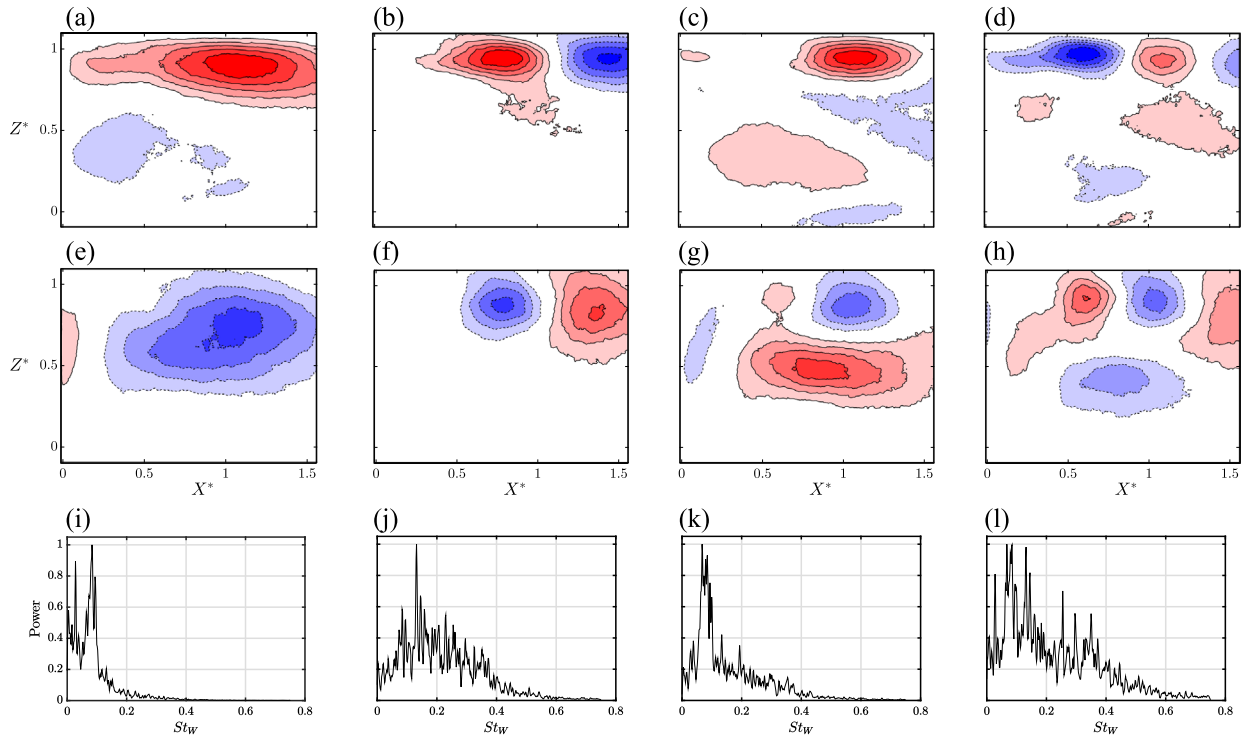

Fig. 21. Proper Orthogonal Decomposition of the $Y^* = 0$ plane. *U* velocity modes 1:4 (a–d), *W* velocity modes 1:4 (e–h), normalised power spectra of the mode coefficient, modes 1:4 (i–l). Contours normalised by peak mode component.

3.7. *Effect of ground clearance*

In order to assess the influence of the proximity of the under body of the model to the ground plane on the near wake, velocity measurements were taken in the $Y^* = 0$ plane, while the ground clearance was varied from the baseline value of $G^* = 0.14$ up to a maximum of $G^* = 1.1$ and down to a minimum ground clearance of $G^* \approx 0.03$. For all ground clearance values above $G^* = 0.14$ the mean flow, at least in the $Y^* = 0$ centreplane, is structurally equivalent to that of the baseline flow. Fig. 22 shows the reference base streamline pattern overlaid with symbols marking the locations of the critical points for 5 different ground clearances between $G^* = 0.14$ and $G^* = 1.1$. The movement of the flow structures with gap height is minimal, indicating that at the baseline position, the model is already above the region of influence of the ground plane. Furthermore, this suggests that the shape of the nose and possibly the blockage caused by the model supports are sufficient to lock the wake into a significantly vertically asymmetric state.

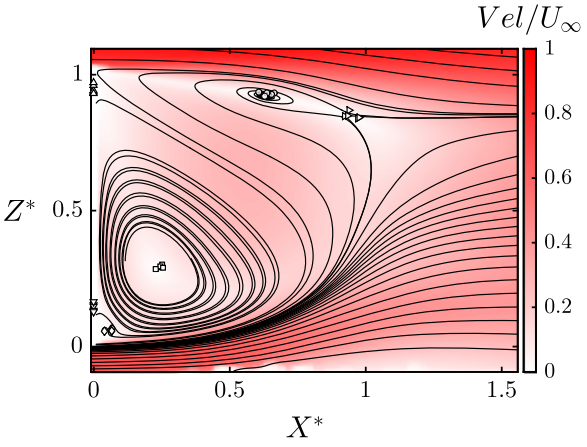

Fig. 22. Time-averaged streamlines for $G^* = 0.14$ together with overlaid critical points in the *xz* symmetry plane. Symbols denote the location of time-averaged critical points for $G^* = 0.28$, 0.42, 0.56, 0.84, 1.1: ◯ upper vortex, □ lower vortex, ⋄ secondary vortex, ▷ saddle point, △ rear stagnation point, ▽ secondary separation point.

When the ground clearance is reduced below the baseline value however, ground plane interactions become apparent, as seen in Fig. 23(a), which shows the mean flow in the $Y^* = 0$ plane for a ground clearance of $G^* = 0.11$. Here, the flow emanating from beneath the body experiences a sufficient adverse pressure gradient that boundary layer separation occurs on the ground plane at $X^* = 0.6$. This produces a vortex centred at $(X^*, Z^*) = (0.88, 0.08)$ and reattachment further downstream at $X^* = 1.22$. This phenomenon is analogous to the separation on the upper channel wall downstream of a backward-facing step with large expansion ratio, as reported by Armaly et al. (1983). The blockage caused by this separation bubble increases the vertical asymmetry of the wake, such that the time-averaged rear stagnation point moves up until it reaches a

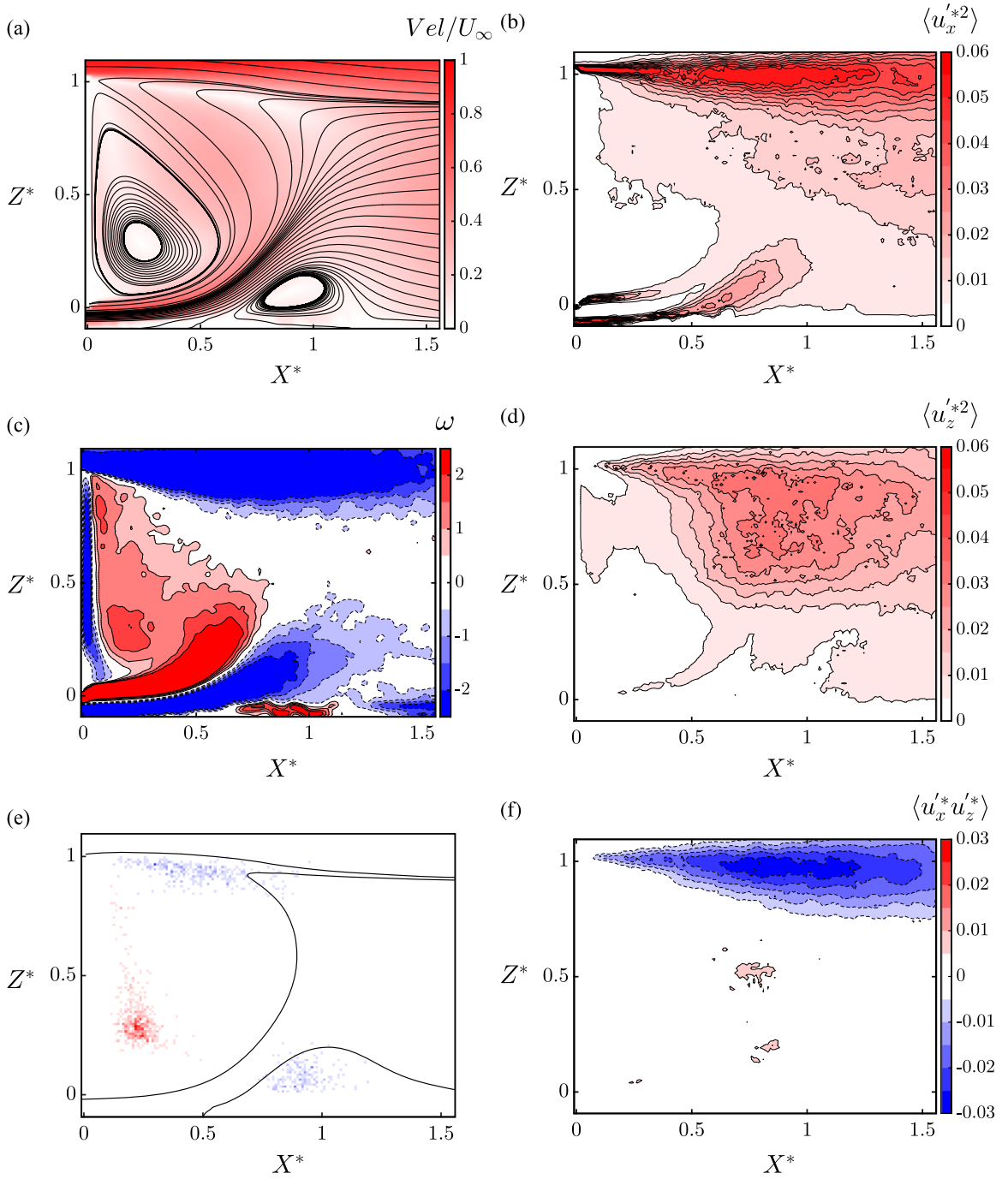

Fig. 23. Ground clearance $G^* = 0.11$, $Y^* = 0$: (a) mean velocity and streamlines, (c) mean vorticity, (e) distribution of instantaneous Γ_1, maximum (red) and minimum (blue), (b) $\langle u_x'^{*2} \rangle$, (d) $\langle u_z'^{*2} \rangle$, (f) $\langle u_x'^{*} u_z'^{*} \rangle$. (For interpretation of the references to colour in this figure caption, the reader is referred to the web version of this paper.)

point indistinguishable from the top of the model. In addition, the time-averaged upper main vortex is no longer detected. The time-averaged Reynolds stress components (Fig. 23b,d,f) show similarities to the baseline case, with added regions of non-negligible $\langle u_x'^{*2}\rangle$ associated with the flow separating from the ground plane. The vorticity distribution (Fig. 23c) shows that due to cross-annihilation between vorticity generated on the lower side of the model and the ground boundary layer, the peak vorticity in the lower shear layer follows a more curved path upwards. The Γ_1 distribution in Fig. 23(e) shows that despite the absence of a time-averaged vortex in the upper region of the wake, from an instantaneous point of view, the upper shear layer still contains a similar distribution of negatively signed vortices. In addition, a cluster of vortices are located in the region of ground-plane separation.

With ground clearance reduced further to $G^* = 0.07$ the underbody flow is fed into the main lower vortex, with ground boundary layer flow reversed between $0.25 \lesssim X^* \lesssim 1.15$. The upper vortex, saddle point and rear stagnation point again return and a node source point becomes apparent at $(X^*, Z^*) = (1.0, 0.37)$. This shows that the wake closure mechanism in this region is dominated by mass flow from the sides of the body rather than flow from the top and that the flow downstream of this area as well as some of the reversed flow that enters the wake originates from the sides of the vehicle. This topology appears consistent with Barlow et al. (2000) who observed a waist in the symmetry plane streamlines for a square back body of aspect ratio 1.44 in ground proximity, although was unable to measure reversed flow with the multi-hole pressure probes used.

The three Reynolds stress components are weakened and deflected downwards (Fig. 24b,d,f). The vorticity plot in Fig. 24 (c) shows that the positively signed vorticity generated on the underside of the vehicle is fed exclusively into the main lower vortex, and as a result, the lower vortex at $G^* = 0.07$ is stronger that the one at $G^* = 0.11$. Fig. 24(e) shows that the locations

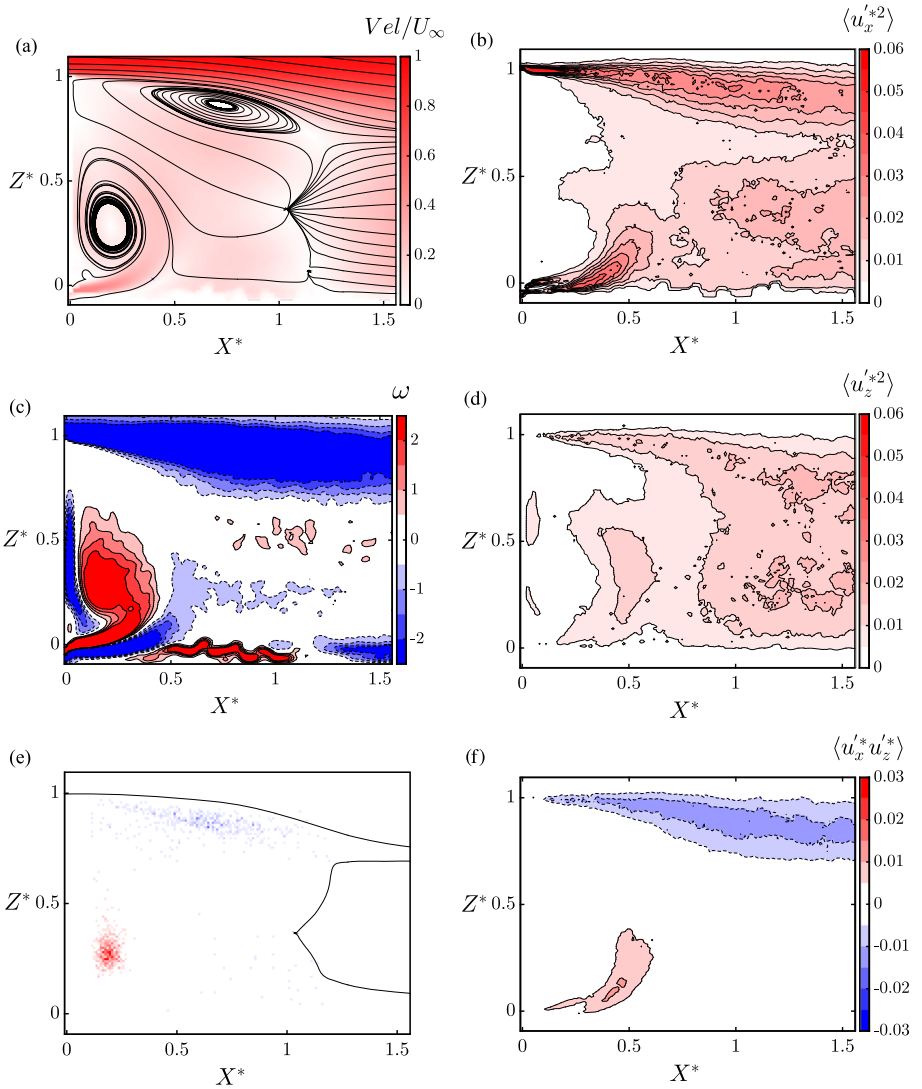

Fig. 24. Ground clearance $G^* = 0.07$, $Y^* = 0$: (a) mean velocity and streamlines, (c) mean vorticity, (e) distribution of instantaneous Γ_1, maximum (red) and minimum (blue), (b) $\langle u_x'^{*2}\rangle$, (d) $\langle u_z'^{*2}\rangle$, (f) $\langle u_x'^{*} u_z'^{*}\rangle$. (For interpretation of the references to colour in this figure caption, the reader is referred to the web version of this paper.)

of the most intense vortices remain similar to those at higher ground clearance.

The lowest ground clearance achievable was $G^* \simeq 0.03$, owing to the fillets between the supports and the bottom of the model. In this configuration the upper region of the wake undergoes a significant topology change. The time averaged upper vortex (Fig. 25a) is enlarged and moved downwards and upstream. It can be seen from the vorticity contours in Fig. 25 (c) and the vortex centre histogram in Fig. 25(e) that this structure is no longer located within the upper shear layer. The upper vortex now has similar properties to the lower vortex in the baseline case in terms of position, size and stability. Although not entirely suppressed, the formation of Kelvin–Helmholtz vortices in the upper shear layer is reduced, leading to

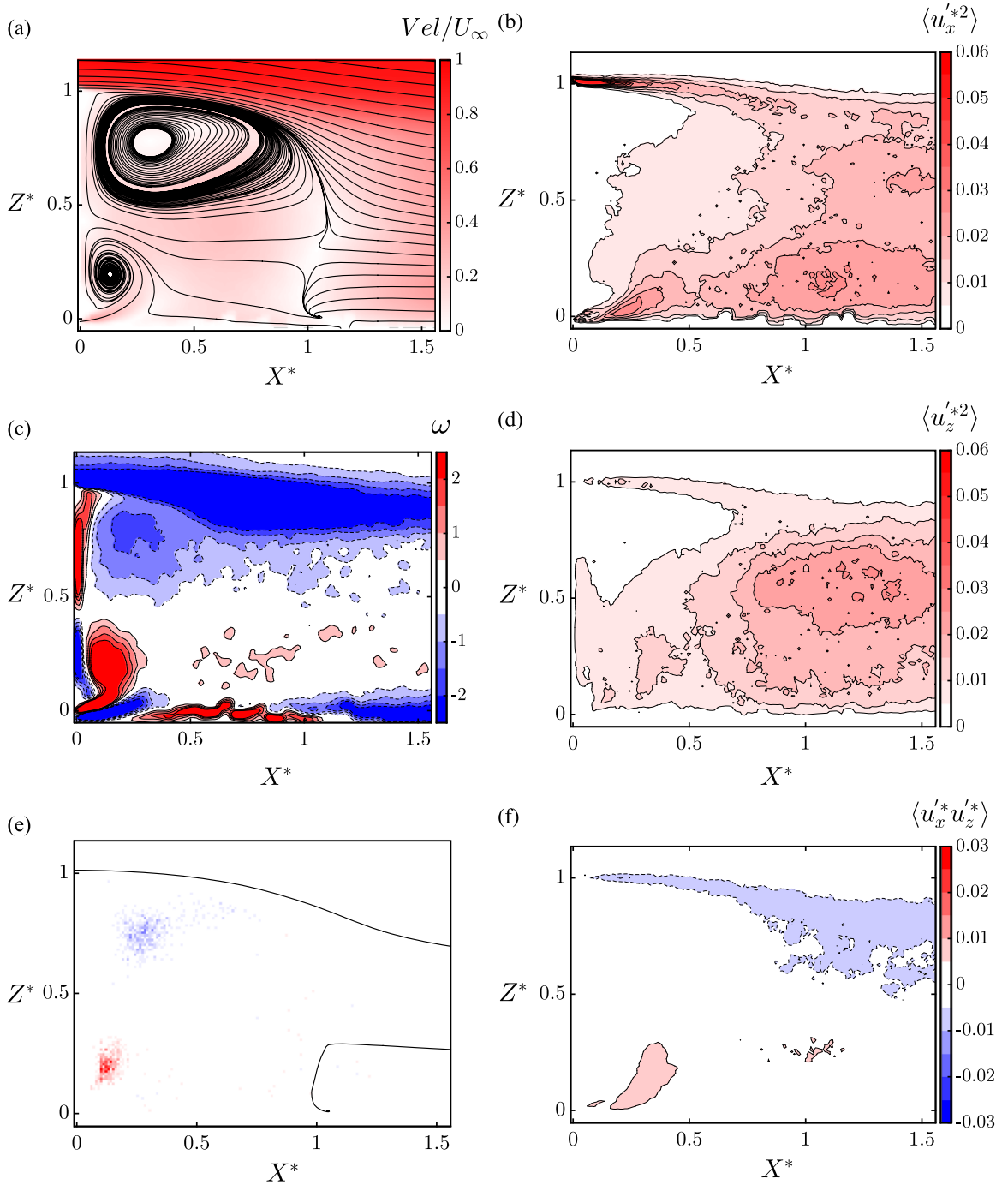

Fig. 25. Ground clearance $G^* = 0.03$, $Y^* = 0$: (a) mean velocity and streamlines, (c) mean vorticity, (e) distribution of instantaneous Γ_1, maximum (red) and minimum (blue), (b) $\langle u_x'^{*2} \rangle$, (d) $\langle u_z'^{*2} \rangle$, (f) $\langle u_x'^{*} u_z'^{*} \rangle$. (For interpretation of the references to colour in this figure caption, the reader is referred to the web version of this paper.)

a decrease in all 3 Reynolds stress components in that region (Fig. 25b,d,f). Due to the reduced underbody flow, the main lower vortex in this case has moved closer to the base of the vehicle but still retains a high level of vorticity.

The streamlines bounding the time-averaged recirculating region are near vertical for $0 < Z^* < 0.5$, suggesting once again that inflow from the sides of the model is the dominant wake closure mechanism. This behaviour is different to that presented in Wang et al. (2013) for 25° and 35° Ahmed bodies with zero ground clearance. In that work, the contour of zero streamwise velocity in the $Y^* = 0$ plane extends from near the base of the vehicle to the reattachment point on the ground plane at a significant angle to the vertical. This suggests that flow over the roof of the model is the dominant mechanism responsible for the wake closure. The difference can be attributed both to the lower aspect ratio and slanted roof on the Ahmed body.

While the effect of reduced ground clearance has been shown to cause a significant modification to the mean symmetry plane flow topology; the main lower vortex continues to be relatively stable and remains in close proximity to the base of the model. This suggests that even at low ground clearances it remains a significant source of base suction.

4. Conclusions

The flow around the generic *Ground Transportation System* heavy vehicle model has been characterised at a Reynolds number of 2.7×10^4. Despite this relatively low Reynolds number compared with real-world operating trucks, there is good agreement with results reported in the literature at significantly higher Reynolds numbers, largely due to the square-backed geometry with fixed separation lines. It is shown that the time-averaged near wake displays a high level of vertical asymmetry, with the lower part of the wake being dominated by a large quasi-stationary spanwise vortex. The positioning of this vortex corresponds with the peak negative base pressure reported elsewhere in the literature. Reducing ground clearance was found to cause significant changes in both steady state and transient wake topology, with the wake becoming fully attached to the ground plane and the main upper vortex transitioning to an almost quasi-steady state, similar to the main lower vortex of the baseline case. Despite this, for the lower section of the near wake the lower vortex persisted and remained in close proximity to the base of the vehicle, suggesting it continues to be a source of base suction.

Using a series of PIV velocity measurements in orthogonal planes, a three-dimensional map of streamwise fluctuations was constructed, indicating that the dominant fluctuating energy, and unassociated unsteadiness, is contained within the upper- and side-shear layers. Fourier transforms and Proper Orthogonal Decomposition were used to characterise these fluctuations, confirming that the dominant modes of the wake fluctuated at reduced frequencies of $St \approx 0.08$ and 0.17, corresponding to a wake pumping mode, and horizontal shedding between the sides of the wake. The lower vortex on the other hand was found to be very stable, in terms of both position and time.

Acknowledgements

DM gratefully acknowledges scholarship and project support from ARC Linkage Project grant LP0991170.

Appendix A. Comparison of mean velocity fields to Storms et al. (2001)

This section contains a comparison between the mean flow topology from the current study and the work of Storms et al. (2001), conducted at a $Re_W = 2 \times 10^6$ using 3 component PIV. The data was taken from images in Roy et al. (2006) and manually fitted to the same axes as used throughout this paper. Good agreement is shown between the two, despite the large difference in Reynolds number (Figs. 26 and 27).

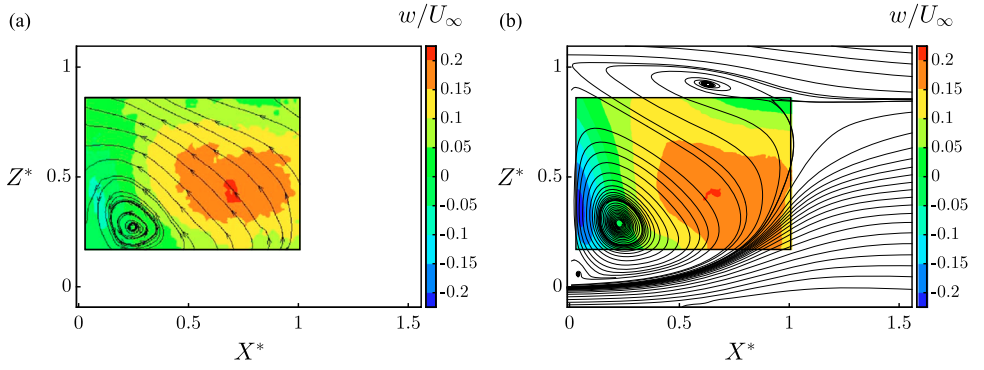

Fig. 26. Time averaged streamlines and contours of vertical velocity w in the plane $Y^* = 0$. (a) Storms et al. (2001) reproduced from Roy et al. (2006), $Re_W = 2.0 \times 10^6$. (b) Current study, $Re_W = 2.7 \times 10^4$.

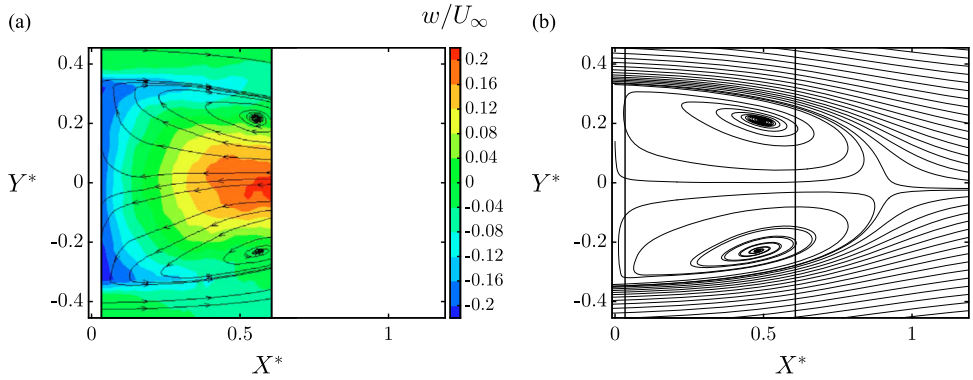

Fig. 27. Time averaged streamlines and contours of vertical velocity w in the plane $Z^* = 0.5$. (a) Storms et al. (2001) reproduced from Roy et al. (2006), $Re_W = 2.0 \times 10^6$. (b) Time averaged streamlines from current study, $Re_W = 2.7 \times 10^4$.

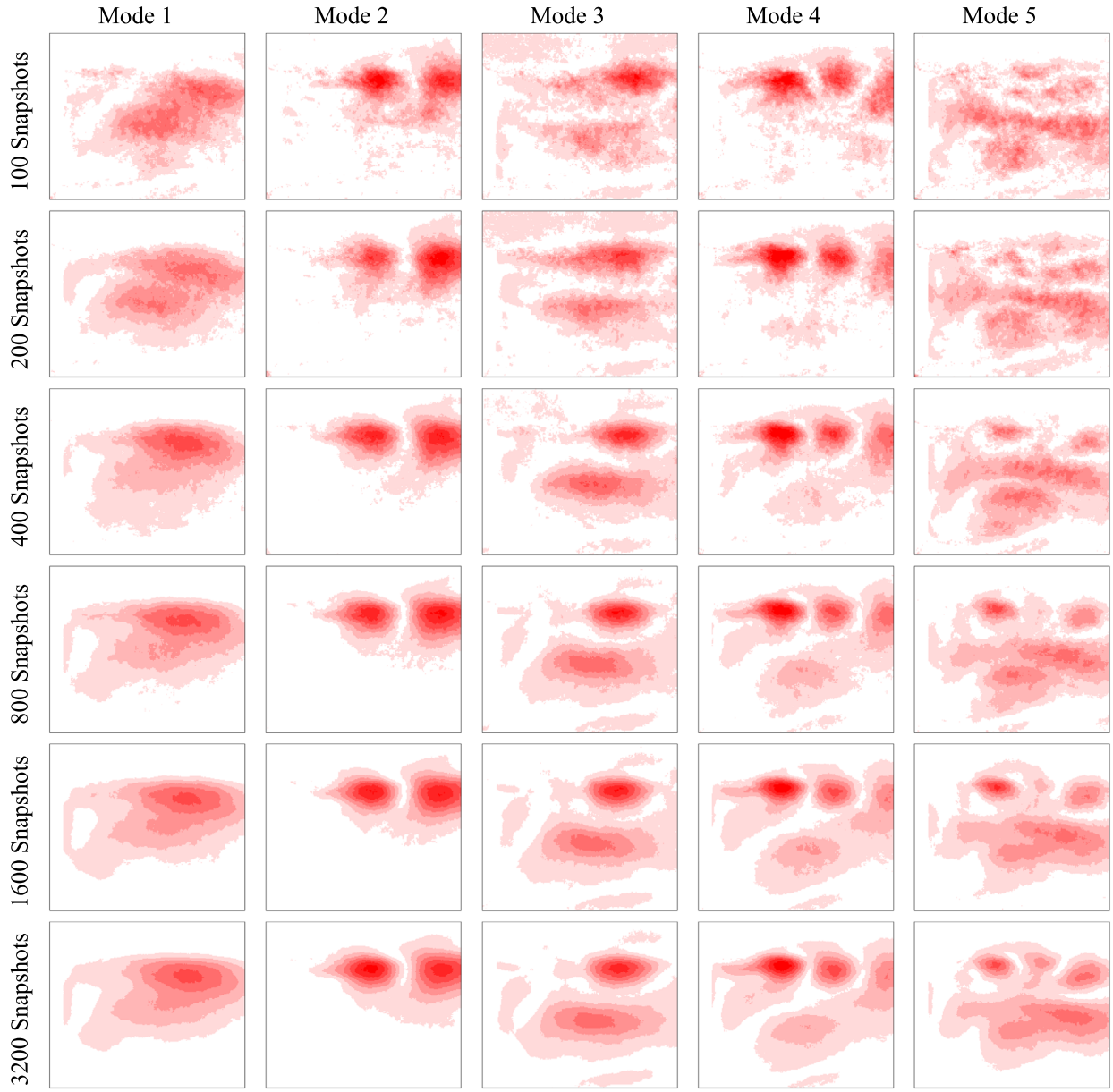

Fig. 28. Velocity magnitude fields of the first 5 unsteady POD modes in the $Y^* = 0$ plane showing the changes induced by varying the number of snapshots used. Decomposition of 100, 200, 400, 800, 1600 and 3200 snapshots.

Appendix B. Effect on POD of the number of velocity field snapshots

This appendix shows the influence of changing the number of velocity snapshots used to extract the dominant POD modes. The number of snapshots was successively increased by a factor of 2 from 100 to 3200, showing that the mode shapes and mode order are maintained faithfully. Beyond $N=400$, there is little visually detectable change in the structure of the top five modes. Nevertheless, the decompositions used for this paper employed at least $N=3200$, to extract the spatial modes in each plane (Fig. 28).

References

Armaly, B.F., Durst, F., Pereira, J., Schönung, B., 1983. Experimental and theoretical investigation of backward-facing step flow. J. Fluid Mech. 127, 473–496.

Barlow, J., Guterres, R., Ranzenbach, R., 2000. Parametric Study of Wake Structures and Forces of Rectangular Bodies with Radiused Edges Near a Plane Surface. Technical Report, SAE Technical Paper.

Basley, J., Pastur, L., Lusseyran, F., Faure, T.M., Delprat, N., 2011. Experimental investigation of global structures in an incompressible cavity flow using time-resolved piv. Exp. Fluids 50 (4), 905–918.

Bearman, P., 1965. Investigation of the flow behind a two-dimensional model with a blunt trailing edge and fitted with splitter plates. J. Fluid Mech. 21 (02), 241–255.

Berkooz, G., Holmes, P., Lumley, J.L., 1993. The proper orthogonal decomposition in the analysis of turbulent flows. Annu. Rev. Fluid Mech. 25 (1), 539–575.

Bruneau, C.-H., Creusé, E., Depeyras, D., Gilliéron, P., Mortazavi, I., 2010. Coupling active and passive techniques to control the flow past the square back Ahmed body. Comput. Fluids 39 (10), 1875–1892.

Burton, D., McArthur, D., Sheridan, J., Thompson, M., 2013. Contribution of add-on components to the aerodynamic drag of a cab-over truck-trailer combination vehicle. SAE Int. J. Commer. Veh. 6 (September), 477–485, http://dx.doi.org/10.4271/2013-01-2428.

Burton, D., Nazarinia, M., Sheridan, J., Parkin, D., 2011. Optimisation of boat-tails for heavy vehicles. In: ASME-JSME-KSME 2011 Joint Fluids Engineering Conference. American Society of Mechanical Engineers, Hamamatsu, Japan, pp. 885–891.

Cooper, K.R., 2012. Wind tunnel and track tests of class 8 tractors pulling single and tandem trailers fitted with side skirts and boat-tails. SAE Int. J. Commer. Veh. 5 (April), 1–17, http://dx.doi.org/10.4271/2012-01-0104.

Croll, R.H., Gutierrez, W.T., Hassan, B., Suazo, J.E., Riggins, A.J., 1996. Experimental Investigation of the Ground Transportation Systems (gts) Project for Heavy Vehicle Drag Reduction. Technical Report, SAE Technical Paper.

Duell, E.G., George, A.R., 1999. Experimental Study of a Ground Vehicle Body Unsteady Near Wake. SAE Technical Paper, SAE International (March), http://dx.doi.org/10.4271/1999-01-0812.

Fouras, A., Jacono, D.L., Hourigan, K., 2008. Target-free stereo piv: a novel technique with inherent error estimation and improved accuracy. Exp. Fluids 44 (2), 317–329.

Fouras, A., Soria, J., 1998. Accuracy of out-of-plane vorticity measurements derived from in-plane velocity field data. Exp. Fluids 25 (5–6), 409–430.

Gerrard, J., 1966. The mechanics of the formation region of vortices behind bluff bodies. J. Fluid Mech. 25 (02), 401–413.

Ghias, R., Khondge, A., Sovani, S.D., 2008. Flow Simulations Around a Generic Ground Transportation System: Using Immersed Boundary Method. Technical Report, SAE Technical Paper.

Graftieaux, L., Michard, M., Grosjean, N., 2001. Combining piv, pod and vortex identification algorithms for the study of unsteady turbulent swirling flows. Meas. Sci. Technol. 12 (9), 1422.

Grandemange, M., Gohlke, M., Cadot, O., 2013a. Bi-stability in the turbulent wake past parallelepiped bodies with various aspect ratios and wall effects. Phys. Fluids (1994–present) 25 (9), 095103.

Grandemange, M., Gohlke, M., Cadot, O., 2013b. Turbulent wake past a three-dimensional blunt body. Part 1. Global modes and bi-stability. J. Fluid Mech. 722, 51–84.

Grandemange, M., Gohlke, M., Cadot, O., 2014. Turbulent wake past a three-dimensional blunt body. Part 2. Experimental sensitivity analysis. J. Fluid Mech. 752, 439–461.

Han, T., Hammond, D., Sagi, C., 1992. Optimization of bluff body for minimum drag in ground proximity. AIAA J. 30 (4), 882–889.

Heineck, J.T., Walker, S.M., 1999. 3d piv in Wind Tunnel Applications: Measurements of a Truck Wake. Technical Report, SAE Technical Paper.

Hoerner, S.F., 1965. Fluid-Dynamic Drag: Practical Information on Aerodynamic Drag and Hydrodynamic Resistance. Hoerner Fluid Dynamics Midland Park, NJ.

Hucho, Wolf-Heinrich. Aerodynamics of Road Vehicles: From Fluid Mechanics to Vehicle Engineering, W. SAE International, Warrendale, PA 177,1998, ISBN: 0-7680-0029-7.

Kehs, J.P., Visser, K.D., Grossman, J., Niemiec, J., Smith, A., Horrell, C.M., 2013. A comparison of full scale aft cavity drag reduction concepts with equivalent wind tunnel test results. SAE Int. J. Commer. Veh. 6 (September), 486–497, http://dx.doi.org/10.4271/2013-01-2429.

Khalighi, B., Chen, K.-H., Iaccarino, G., 2012. Unsteady aerodynamic flow investigation around a simplified square-back road vehicle with drag reduction devices. J. Fluids Eng. 134 (6), 061101.

Khalighi, B., Zhang, S., Koromilas, C., Balkanyi, S., Bernal, L.P., Iaccarino, G., Moin, P., 2001. Experimental and Computational Study of Unsteady Wake Flow Behind a Bluff Body with a Drag Reduction Device. Technical Report, SAE Technical Paper.

Landman, D., Wood, R., Seay, W., Bledsoe, J., 2009. Understanding practical limits to heavy truck drag reduction. SAE Int. J. Commer. Veh. 2 (October), 183–190, http://dx.doi.org/10.4271/2009-01-2890.

Leuschen, J., Cooper, K.R., 2006. Full-scale Wind Tunnel Tests of Production and Prototype, Second-generation Aerodynamic Drag-reducing Devices for Tractor-trailers. SAE Technical Paper, SAE International (October), http://dx.doi.org/10.4271/2006-01-3456.

Liou, W.W., 1994. Linear instability of curved free shear layers. Phys. Fluids (1994–present) 6 (2), 541–549.

Littlewood, R., Passmore, M., 2010. The Optimization of Roof Trailing Edge Geometry of a Simple Square-back. Technical Report, SAE Technical Paper.

Maddox, S., Squires, K.D., Wurtzler, K.E., Forsythe, J.R., 2004. Detached-eddy simulation of the ground transportation system. In: The Aerodynamics of Heavy Vehicles: Trucks, Buses, and Trains. Springer, pp. 89–104.

Mariotti, A., Buresti, G., 2013. Experimental investigation on the influence of boundary layer thickness on the base pressure and near-wake flow features of an axisymmetric blunt-based body. Exp. Fluids 54 (11), 1–16.

Martini, H., Bergqvist, B., Hjelm, L., Lfdahl, L., 2011. Aerodynamic Effects of Roof Deflector and Cab Side Extenders for Truck-trailer Combinations. SAE Technical Paper, SAE International (September), http://dx.doi.org/10.4271/2011-01-2284.

McCallen, R., Couch, R., Hsu, J., Browand, F., Hammache, M., Leonard, A., Brady, M., Salari, K., Rutledge, W., Ross, J., Storms, B., Heineck, J., Driver, D., Bell, J., Zilliac, G., 1999. Progress in Reducing Aerodynamic Drag for Higher Efficiency of Heavy Duty Trucks (class 7–8). SAE Technical Paper, SAE International (April), http://dx.doi.org/10.4271/1999-01-2238.

Ortega, J.M., Dunn, T., McCallen, R., Salari, K., 2004. Computational simulation of a heavy vehicle trailer wake. The Aerodynamics of Heavy Vehicles: Trucks, Buses, and Trains. Springer, Berlin Heidelberg, 219–233.

Ortega, J.M., Salari, K., 2008. Investigation of a Trailer Underbody Fairing for Heavy Vehicle Aerodynamic Drag Reduction. SAE Technical Paper, SAE International (October), http://dx.doi.org/10.4271/2008-01-2601.

Östh, J., Noack, B.R., Krajnović, S., Barros, D., Borée, J., 2014. On the need for a nonlinear subscale turbulence term in pod models as exemplified for a high-

Reynolds-number flow over an Ahmed body. J. Fluid Mech. 747, 518–544.
Parkin, D., Sheridan, J., Thompson, M., 2015. Numerical analysis of periodic open-loop flow control on bluff bodies in ground proximity. J. Wind Eng. Ind. Aerodyn. 145, 339–350. URL ⟨⟩.
Parkin, D.J., Thompson, M., Sheridan, J., 2014. Numerical analysis of bluff body wakes under periodic open-loop control. J. Fluid Mech. 739, 94–123.
Pastoor, M., Henning, L., Noack, B.R., King, R., Tadmor, G., 2008. Feedback shear layer control for bluff body drag reduction. J. Fluid Mech. 608, 161–196.
Phersson, L., Sheridan, J., Thompson, M., Burton, D., 2014. Effect of sinusoidal forcing on bluff body drag. In: Proceedings of Numerical and Experimental Aerodynamics of Road Vehicles and Trains (AEROVEHICLES1).
Rayleigh, L., 1917. On the dynamics of revolving fluids. Proc. R. Soc. Lond. Ser. A: Contain. Pap. Math. Phys. Charac. 93 (648), 148–154.
Roshko, A., 1955. On the wake and drag of bluff bodies. J. Aeronaut. Sci. (Inst. Aeronaut. Sci.) 22 (2).
Roy, Christopher, J., Harshavardhan, A. Ghuge., 2009. Detached eddy simulations of a simplified tractor/trailer geometry. The Aerodynamics of Heavy Vehicles II: Trucks, Buses, and Trains. Springer Berlin Heidelberg, 363–381.
Roy, C.J., Payne, J., McWherter-Payne, M., 2006. Rans simulations of a simplified tractor/trailer geometry. J. Fluids Eng. 128 (5), 1083–1089.
Storms, B.L., Ross, J.C., Heineck, J.T., Walker, S.M., Driver, D.M., Zilliac, G.G., 2001. An experimental study of the ground transportation system (GTS) model in the NASA ames 7-by-10-ft wind tunnel. National Aeronautics and Space Administration, Ames Research Center.
Unaune, S.V., Sovani, S.D., Kim, S.E., 2005. Aerodynamics of a Generic Ground Transportation System: Detached Eddy Simulation. Technical Report, SAE Technical Paper.
Van Oudheusden, B., Scarano, F., Van Hinsberg, N., Watt, D., 2005. Phase-resolved characterization of vortex shedding in the near wake of a square-section cylinder at incidence. Exp. Fluids 39 (1), 86–98.
Volpe, R., Devinant, P., Kourta, A., 2014. Unsteady experimental characterization of the natural wake of a squareback ahmed model. In: ASME 2014 4th Joint US-European Fluids Engineering Division Summer Meeting Collocated with the ASME 2014 12th International Conference on Nanochannels, Microchannels, and Minichannels. American Society of Mechanical Engineers, pp. V01CT17A007–V01CT17A007.
Wang, X., Zhou, Y., Pin, Y., Chan, T., 2013. Turbulent near wake of an Ahmed vehicle model. Exp. Fluids 54 (4), 1–19.
Zhang, B., Zhou, Y., To, S., 2015. Unsteady flow structures around a high-drag Ahmed body. J. Fluid Mech. 777, 291–326.